

## Journal of Geophysical Research: Atmospheres

## RESEARCH ARTICLE

10.1002/2017JD027006

## Special Section:

Simulations of Stratospheric Sulfate Aerosol Geoengineering with the Whole Atmosphere Community Climate Model (WACCM)

This article is a companion to MacMartin et al. (2017), <https://doi.org/10.1002/2017JD026868>, Richter et al. (2017), <https://doi.org/10.1002/2017JD026912>, Kravitz et al. (2017), <https://doi.org/10.1002/2017JD026874>, and Tilmes et al. (2017), <https://doi.org/10.1002/2017JD026888>.

## Key Points:

- WACCM accurately calculates radiative and chemical responses to stratospheric sulfate, validating its use for geoengineering studies
- Interactive OH chemistry is key to the study of aerosol formation from large stratospheric SO<sub>2</sub> perturbations
- OH depletion extended the calculated average initial e-folding time for oxidation of SO<sub>2</sub> from the 1991 Pinatubo eruption by >50%

## Supporting Information:

- Supporting Information S1
- Table S1

## Correspondence to:

M. J. Mills,  
mmills@ucar.edu

## Citation:

Mills, M. J., Richter, J. H., Tilmes, S., Kravitz, B., MacMartin, D. G., Glanville, A. A., ... Kinnison, D. E. (2017). Radiative and chemical response to interactive stratospheric sulfate aerosols in fully coupled CESM1(WACCM). *Journal of Geophysical Research: Atmospheres*, 122. <https://doi.org/10.1002/2017JD027006>

Received 20 APR 2017

Accepted 23 OCT 2017

Accepted article online 6 NOV 2017

## Radiative and Chemical Response to Interactive Stratospheric Sulfate Aerosols in Fully Coupled CESM1(WACCM)

Michael J. Mills<sup>1</sup> , Jadwiga H. Richter<sup>2</sup> , Simone Tilmes<sup>1,2</sup> , Ben Kravitz<sup>3</sup> , Douglas G. MacMartin<sup>4,5</sup> , Anne A. Glanville<sup>1</sup> , Joseph J. Tribbia<sup>2</sup> , Jean-François Lamarque<sup>1,2</sup> , Francis Vitt<sup>1</sup> , Anja Schmidt<sup>6,7,8</sup> , Andrew Gettelman<sup>1,2</sup> , Cecile Hannay<sup>2</sup> , Julio T. Bacmeister<sup>2</sup> , and Douglas E. Kinnison<sup>1</sup> 

<sup>1</sup>Atmospheric Chemistry, Observations and Modeling Laboratory, National Center for Atmospheric Research, Boulder, CO, USA, <sup>2</sup>Climate and Global Dynamics Laboratory, National Center for Atmospheric Research, Boulder, CO, USA, <sup>3</sup>Pacific Northwest National Laboratory, Richland, WA, USA, <sup>4</sup>Mechanical and Aerospace Engineering, Cornell University, Ithaca, NY, USA, <sup>5</sup>Department of Computing and Mathematical Sciences, California Institute of Technology, Pasadena, CA, USA, <sup>6</sup>School of Earth and Environment, University of Leeds, Leeds, UK, <sup>7</sup>Department of Chemistry, University of Cambridge, Cambridge, UK, <sup>8</sup>Department of Geography, University of Cambridge, Cambridge, UK

**Abstract** We present new insights into the evolution and interactions of stratospheric aerosol using an updated version of the Whole Atmosphere Community Climate Model (WACCM). Improved horizontal resolution, dynamics, and chemistry now produce an internally generated quasi-biennial oscillation and significant improvements to stratospheric temperatures and ozone compared to observations. We present a validation of WACCM column ozone and climate calculations against observations. The prognostic treatment of stratospheric sulfate aerosols accurately represents the evolution of stratospheric aerosol optical depth and perturbations to solar and longwave radiation following the June 1991 eruption of Mount Pinatubo. We confirm the inclusion of interactive OH chemistry as an important factor in the formation and initial distribution of aerosol following large inputs of sulfur dioxide (SO<sub>2</sub>) to the stratosphere. We calculate that depletion of OH levels within the dense SO<sub>2</sub> cloud in the first weeks following the Pinatubo eruption significantly prolonged the average initial e-folding decay time for SO<sub>2</sub> oxidation to 47 days. Previous observational and model studies showing a 30 day decay time have not accounted for the large (30–55%) losses of SO<sub>2</sub> on ash and ice within 7–9 days posteruption and have not correctly accounted for OH depletion. We examine the variability of aerosol evolution in free-running climate simulations due to meteorology, with comparison to simulations nudged with specified dynamics. We assess calculated impacts of volcanic aerosols on ozone loss with comparisons to observations. The completeness of the chemistry, dynamics, and aerosol microphysics in WACCM qualify it for studies of stratospheric sulfate aerosol geoengineering.

**Plain Language Summary** Stratospheric aerosols form after volcanoes inject SO<sub>2</sub> into the stratosphere, and can cool global surface temperatures. A new capability for simulating stratospheric aerosols from SO<sub>2</sub> injections in the Whole Atmosphere Community Climate Model is shown to reproduce well observed climate and chemistry responses. The ability of the model to calculate accurately the reductions in sunlight and losses of ozone that have been observed following historical eruptions in the satellite era gives strong confidence in the model's ability to simulate such responses to potential future deliberate injections of SO<sub>2</sub> to offset global warming. Such responses to geoengineering are presented in a series of companion papers.

### 1. Introduction

In this study, we describe a new version of an Earth system model capable of representing the formation and interactions of stratospheric sulfate aerosol from source gases and use it to study the evolution and radiative and chemical impacts of SO<sub>2</sub> inputs from large volcanic eruptions. We use this model in a series of companion papers (Kravitz et al., 2017; MacMartin et al., 2017; Richter et al., 2017; Tilmes et al., 2017) to study the effects of different stratospheric sulfate geoengineering strategies. The detailed comparisons to observations presented here establish confidence in this model and provide new insights into the role of interactive chemistry in the evolution of dense SO<sub>2</sub> clouds in the stratosphere.

Geoengineering, also known as climate engineering, describes a set of technologies designed to offset some of the effects of anthropogenic greenhouse gas emissions (McNutt et al., 2015). There are many proposed methods of offsetting anthropogenic climate change, and one method that has arguably received the most attention is stratospheric sulfate aerosol geoengineering (Budyko, 1977; Crutzen, 2006). This method involves injecting large amounts of sulfur-bearing precursor gases, often sulfur dioxide ( $\text{SO}_2$ ), into the stratosphere. These gases then photochemically convert to highly reflective sulfate aerosols, which scatter sunlight back to space, cooling the Earth's surface and lower atmosphere.

The idea of stratospheric sulfate aerosol geoengineering has gained the most traction of all proposed methods because of its natural analogue of large volcanic eruptions. Such volcanic eruptions similarly enhance the stratospheric sulfate aerosol layer, resulting in a cooling of Earth's climate that can last several years (e.g., Robock, 2000). The 1815 eruption of Mount Tambora in what is now Indonesia was followed by the "year without a summer" in 1816 in New England and Europe—which extended to several years in China—as well as severe disruptions to the Indian monsoon and to other global climate patterns (Raible et al., 2016; Wood, 2014). The 1991 eruption of Mount Pinatubo (15.1°N, 120.3°E) produced a rapid global-averaged cooling at the Earth's surface of several tenths of a degree Celsius over the following year, despite the significant warming effects of a coincident El Niño event (Bender et al., 2010; Hansen et al., 1992; Soden et al., 2002).

Accurately simulating the climate effects of large volcanic eruptions, and in turn stratospheric sulfate aerosol geoengineering, in a climate model requires the model to simulate processes that represent all the components of sulfate aerosol formation and microphysical growth; interaction of aerosols with radiation, dynamics, and chemistry; and sedimentation of the aerosols. Only recently have climate models included these processes, to allow for the interactive simulation of stratospheric sulfate aerosol evolution based on emissions of sulfur-bearing precursor gases. Inclusion of these processes has been shown to greatly improve the treatment of volcanic aerosol properties and their effects on stratospheric chemistry compared to observations (English et al., 2013; Ivy et al., 2017; Mills et al., 2016; Solomon et al., 2016; Timmreck et al., 1999). In addition, simulation of the interactions between stratospheric processes and surface climate requires coupling to an ocean and sea ice model, which is often lacking in models with prognostic aerosol capabilities. These processes are essential for studying the atmospheric and surface climate impacts of stratospheric sulfate aerosol geoengineering.

We describe an updated version of the Earth system model described in Mills et al. (2016) with the above processes and interactions included. Updates include increased horizontal resolution and a self-generating quasi-biennial oscillation (QBO). We use this model here to study the chemical, microphysical, and radiative effects of historical volcanic eruptions that have occurred during the satellite era (1979 to present), with comparison to observations. We demonstrate the importance of interactive calculations of the abundance of oxidants, such as the hydroxyl radical ( $\text{OH}$ ), to understanding the observations of  $\text{SO}_2$  evolution following large volcanic eruptions.

## 2. Materials and Methods

### 2.1. Whole Atmosphere Community Climate Model

The Community Earth System Model, version 1 (CESM1, Hurrell et al., 2013), is a state-of-the-art global climate model that includes interactive atmosphere, ocean, land, and sea ice components. The atmosphere component of CESM1 is the Community Atmosphere Model (CAM), which includes a high-top version known as the Whole Atmosphere Community Climate Model (WACCM, Marsh et al., 2013). Mills et al. (2016) describe the development of a prognostic treatment of stratospheric sulfate aerosol in CESM1(WACCM) with the more realistic formulations of radiation, planetary boundary layer turbulence, cloud microphysics, and aerosols that were introduced in version 5 of CAM (Neale et al., 2010). Mills et al. (2016) presented and validated volcanic aerosol properties derived from  $\text{SO}_2$  emissions over the period 1990–2014 but did not examine radiative forcing. In this paper, we validate radiative forcing from volcanic aerosol following the 1991 Pinatubo eruption calculated with WACCM. Such validation is critical for the use of this model in studies of the radiative impacts of stratospheric sulfate aerosol derived from  $\text{SO}_2$  emissions. The horizontal resolution of the atmosphere component in this model, which we call WACCM hereafter, is  $0.95^\circ$  latitude  $\times 1.25^\circ$  longitude, which is double the resolution in each horizontal dimension of previous versions of CESM1(WACCM) (Marsh et al., 2013; Mills et al., 2016).

WACCM extends from the Earth's surface to 140 km in altitude. In our configuration, WACCM includes comprehensive, fully interactive middle atmosphere chemistry with 95 solution species, 2 invariant species, 91 photolysis reactions, and 207 other reactions. The chemical scheme includes gas phase chemical species in the  $O_x$ ,  $NO_x$ ,  $HO_x$ ,  $ClO_x$ , and  $BrO_x$  chemical families, along with  $CH_4$  and its degradation products, and the sulfur-bearing gases dimethyl sulfide (DMS), OCS,  $SO_2$ , SO, S,  $SO_3$ , and  $H_2SO_4$ . Gas phase and heterogeneous reactions important in the stratosphere are included, allowing simulation of the impacts of sulfate aerosols on the chemical composition of the atmosphere, such as the seasonal ozone hole over Antarctica in austral spring (Mills et al., 2016). Our model's middle atmosphere chemistry is a subset of the chemistry used in Mills et al. (2016), excluding species and reactions that are significant only in the troposphere. The reduced chemistry produces up to 45% more OH in the troposphere than Mills et al. (2016), resulting in slightly reduced tropospheric lifetimes for species such as  $CH_4$  and  $SO_2$ . Climate forcings in WACCM include aerosols (tropospheric and stratospheric, and anthropogenic and natural), solar variability, and time-varying mixing ratios of greenhouse gases (determined by lower boundary conditions and interactive chemistry).

WACCM includes a modal treatment of aerosols that is coupled to cloud microphysics (Liu et al., 2012) and which has been extended to include stratospheric sulfate (Mills et al., 2016). To simulate the formation and evolution of sulfate aerosol prognostically, our chemical mechanism includes precursor sulfur-bearing gases and oxidation pathways producing  $H_2SO_4$ . Source gases include OCS, which is an important source of background stratospheric aerosol, as well as  $SO_2$  from anthropogenic sources. The  $H_2SO_4$  resulting from this oxidation creates new sulfate aerosols by the microphysical processes of nucleation and condensation. The processes of coagulation, evaporation, and sedimentation are included in the aerosol microphysical evolution.

The model that we use includes a number of improvements to CAM5 physics beyond what was used in Mills et al. (2016). We use a new surface topography for the CAM finite-volume dynamical core based on Lauritzen et al. (2015). We include an improved representation of atmospheric dust, including refined physical parameterizations of dust and improved soil erodibility, size distributions, wet deposition, and optics (Albani et al., 2014). The cloud microphysical scheme has been updated to Morrison-Gettelman version 2 (MG2), which includes prognostic precipitation (Gettelman & Morrison, 2015). An error in the energy formulation has been corrected (Williamson et al., 2015). The vertical remapping scheme has been updated to improve energy conservation. In the original implementation, temperature was retrieved from total energy remapping (minus kinetic energy), which was shown to produce significant temperature perturbations at high altitude. In the new implementation, temperature is remapped over a log-pressure coordinate, which preserves the geopotential at the model lid during remapping.

Ice nucleation has been updated to include effects of preexisting ice crystals and to consider in-cloud variability in ice saturation ratio (Shi et al., 2015). The ice nucleation scheme was developed for the troposphere and contains several assumptions that may adversely affect ice nucleation in the upper troposphere and lower stratosphere in our model. The heterogeneous ice nucleation code assumes that only dust aerosols nucleate ice and only those in the larger of the two dust aerosol modes. In deriving the fraction of dust in this coarse mode, the code considers only the ratio of dust to sea salt, neglecting the presence of sulfates in the coarse mode. Thus, in the upper troposphere and stratosphere, where sulfate dominates aerosol composition, the very small dust fraction is greatly overestimated because the sea salt mass there is small compared to the dust mass. Hence, the code overestimates heterogeneous freezing in the upper troposphere and lower stratosphere, but only in model grid points where dust is present, and hence is not an issue in most of the stratosphere. In addition, coarse aerosols that nucleate ice are not moved to the in-cloud population and are available to nucleate ice each additional time step, leading to further overestimates of heterogeneous freezing. Homogeneous freezing of aerosols is considered only for sulfates in the Aitken mode. The neglect of sulfates in the larger accumulation and coarse modes likely underestimates ice production by homogeneous freezing, particularly under geoengineered conditions. Because the impacts on ice nucleation are compensating, the sign of model biases introduced is unclear. Heterogeneous reactions on stratospheric ice account for a small ( $\sim 1\%$ ) proportion of Antarctic ozone loss. These issues may have more significant impacts on the interaction of aerosols with ice clouds, which can absorb outgoing longwave radiation. The erroneous treatment of sulfates as heterogeneous ice nuclei where dust is present may produce unrealistic increases in cirrus clouds in the upper troposphere under geoengineering conditions, and the resulting longwave

**Table 1**

WACCM Simulations Conducted for This Work

Simulation name	Dynamics	Chemistry	Ocean/sea ice	# of runs	Years per run	Conditions	SO <sub>2</sub> from eruptions
FRPI	Free-running	Interactive	Coupled	1	50	Preindustrial (1850)	No
FRVOLC	Free-running	Interactive	Coupled	4	42	1975–2016	Yes
SDVOLC	Nudged	Interactive	Data	1	27	1990–2016	Yes
SDVC	Nudged	Interactive	Data	1	27	1990–2016	No
SCVOLC	Free-running	Prescribed	Data	1	21	1979–1999	Yes
SCVC	Free-running	Prescribed	Data	1	10	1990–1999	No

absorption would reduce the cooling efficiency of geoengineering unrealistically. These issues will be addressed in future versions of CESM.

Our WACCM configuration includes the same 70 vertical layers as described in Mills et al. (2016). WACCM uses the Lindzen (1981) gravity wave propagation scheme, using gravity wave source specifications for orographic, frontal, and convectively generated gravity waves following Richter et al. (2010). In this version of WACCM, we have increased the efficiency of convectively generated gravity waves generated by convection to 0.40, from 0.10 used in Mills et al. (2016). This change, together with increased horizontal resolution, allows for an internal generation of the QBO. This new development allows for the examination of the effects of SO<sub>2</sub> injections on the QBO, which are presented in Richter et al. (2017), motivated in part by previous work that has suggested that stratospheric sulfate geoengineering could severely alter the QBO (Aquila et al., 2014). Additional tuning of the gravity wave parameterization in WACCM has significantly reduced the bias of the temperatures in the Antarctic polar vortex, which is critical to calculating ozone loss (Garcia et al., 2017).

WACCM is fully coupled to the Community Land Model version 4.0 (CLM4.0, Lawrence et al., 2011). The land model includes interactive carbon and nitrogen cycles, as in CESM1(WACCM) (Marsh et al., 2013). In addition, biogenic surface emissions into the atmosphere are calculated in CLM4.0 using the Model of Emissions of Gases and Aerosols from Nature, version 2.1 (MEGAN2.1, Guenther et al., 2012). WACCM is also coupled to ocean and sea ice components that may be interactive or constrained by data representative of observations. The interactive components are the Parallel Ocean Program, version 2 (POP2, Danabasoglu et al., 2012) and the Los Alamos National Laboratory sea ice model, version 4 (CICE4, Holland et al., 2012).

## 2.2. Model Simulations

Interactive stratospheric aerosol is a new development common to an increasing number of climate models participating in the forthcoming Coupled Model Intercomparison Project, phase 6 (CMIP6, Eyring et al., 2016). Some of these models also include interactive chemistry. Some include an interactive QBO. Interactive aerosols from volcanic eruptions will disperse and evolve differently in different ensemble runs, depending on meteorology (Jones et al., 2016) and the phase of the QBO (Trepte & Hitchman, 1992). We discuss the impacts of these issues on chemistry and climate variability by comparing fully coupled free-running (FR) simulations to those constrained by nudging to specified dynamics (SD). To quantify the importance of interactive chemistry, we conducted two simulations with noninteractive specified chemistry. Table 1 presents a list of simulations performed for this work, each of which is described below. Simulations were carried out on the Yellowstone high-performance computer platform (Computational and Information Systems Laboratory, 2012).

In order to demonstrate radiative balance in the updated model between incoming solar and outgoing long-wave radiation prior to the rapid introduction of anthropogenic greenhouse gases in the industrial era, we first conducted a 50 year preindustrial fully coupled free-running simulation, FRPI, using constant year 1850 climate forcing conditions. The land, ocean, and sea ice components were initialized with the preindustrial equilibrium conditions (1 January, year 402, of the 1850 fully coupled control) used to initialize the CESM1 Large Ensemble simulations (Kay et al., 2015). Initial conditions for the atmosphere are consistent with preindustrial conditions.

Our FRVOLC experiment was designed to examine the model's representation of climate following historical conditions, including volcanic eruptions, from 1975 to 2016, in an ensemble of four fully coupled free-running simulations individually named FRVOLC1, FRVOLC2, FRVOLC3, and FRVOLC4. The land, ocean, and sea ice

components are interactive in these simulations and were initialized with conditions from 1 January 1975 of four independent CESM1 transient simulations used for the Large Ensemble simulation, which were picked to sample contrasting initial ocean states. The atmosphere was initialized with 1 January 1975 conditions from a simulation conducted for the Chemistry Climate Modeling Initiative (Solomon et al., 2015), regressed to our model's higher horizontal resolution, with the addition of spun-up initial conditions for aerosols and sulfur gases from a previous run of our model.

Coupled free-running experiments allow self-consistent representations of stratospheric aerosols, with interactions between atmospheric chemistry and dynamics, and ocean, sea ice, and land. However, the number of unconstrained variable climate states in such simulations poses difficulties for comparisons to observations. Meteorology at the time of volcanic eruption can play an important role in the latitudinal distribution of aerosol, as can the state of the QBO, which can affect the transport of stratospheric aerosol from the tropics to higher latitudes (Trepte & Hitchman, 1992). Ocean states, including the El Niño–Southern Oscillation, strongly affect observations of the Earth's radiation budget, complicating comparisons to coupled free-running simulations. We therefore rely on SD simulations, with prescribed historical sea surface temperatures, and atmospheric winds and temperatures nudged to historical meteorology, to constrain climate variability in WACCM, allowing more detailed comparisons to observations of chemistry and climate responses to stratospheric aerosol.

We performed two SD experiments of the years 1990–2015 using initial conditions from the FRVOLC1 simulation. The SD experiments use meteorological fields from the NASA Global Modeling and Assimilation Office Modern-Era Retrospective Analysis for Research and Applications (MERRA) (Rienecker et al., 2011). Horizontal winds and temperatures are nudged toward the MERRA reanalysis fields between the surface and 50 km, with a relaxation time of 50 h. SDVOLC includes  $\text{SO}_2$  emissions from explosive volcanic eruptions, and SDVC is a “volcanically clean” run without  $\text{SO}_2$  emissions from explosive volcanic eruptions.

Using WACCM, we performed two specified chemistry experiments (Smith et al., 2014), for which chemical oxidants ( $\text{OH}$ ,  $\text{HO}_2$ ,  $\text{O}_3$ , and  $\text{NO}_3$ ) are prescribed. SCVOLC included  $\text{SO}_2$  from volcanic eruptions and simulates years 1979–1999, with an initial condition for 1 January 1979 from FRVOLC1. SCVC does not include  $\text{SO}_2$  from eruptions and simulates years 1990–1999, with an initial condition for 1 January 1990 from SCVOLC. These specified chemistry runs used free-running atmospheric dynamics and prescribed sea surface temperatures and sea ice.

Our FRVOLC, SDVOLC, and SCVOLC experiments use a database of  $\text{SO}_2$  emissions from volcanic eruptions based on version 2 of the Volcanic Emissions for Earth System Models (Neely & Schmidt, 2016). The database includes 222 days of eruption for the years 1975–2016, the dates, spatial coordinates, and  $\text{SO}_2$  mass of which are described in Table S1 of the supporting information. As in Mills et al. (2016), eruptive emissions occur over a 6 h period from 1200 to 1800 UT on the date of the eruption. The climatic phase of the 1991 Pinatubo eruption coincided with the closest pass of Typhoon Yunya (50 km north), which likely affected the initial transport of  $\text{SO}_2$  from the eruption, and which also prevented the retrieval of atmospheric wind profiles during the eruption (Guo, Rose, et al., 2004; Holasek et al., 1996). To account for the observed initial transport of  $\text{SO}_2$  from the Pinatubo eruption southward, we spread the emissions from that eruption evenly between 15.13°N and the equator at 120.3°E, as in previous studies (Dhomse et al., 2014; Mills et al., 2016; Sheng et al., 2015; Timmreck, Graf, & Feichter, 1999; Timmreck, Graf, & Kirchner, 1999). As discussed in Mills et al. (2016), we emit Pinatubo  $\text{SO}_2$  evenly between 18 and 20 km, which allows for self-lofting, giving best agreement with Microwave Limb Sounder (MLS) observations of the  $\text{SO}_2$  cloud (Read et al., 1993).

### 3. Results

#### 3.1. WACCM Climate

As we are presenting a new version of WACCM, we begin by validating the radiative balance of the model in preindustrial conditions, and the climate and chemistry in present-day conditions with respect to observations, before examining volcanic responses. We ignore the first 24 years of the FRPI simulation, to allow the components to equilibrate. The difference between the absorbed solar radiation (ASR) and outgoing longwave radiation (OLR) at the model's top gives a net radiative flux of  $-0.027 \pm 0.442 \text{ W m}^{-2}$  ( $1\sigma$  confidence) over the last 26 years, indicating that the preindustrial atmosphere is in radiative equilibrium.

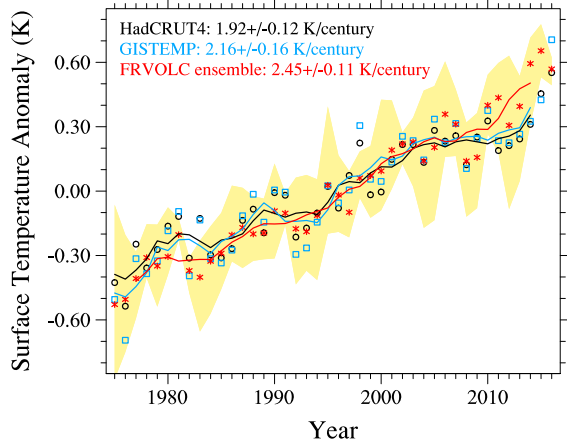


**Figure 1.** Global annual surface temperature anomalies for 1979–2015 from the WACCM FRVOLC ensemble are compared to HadCRUT4 and GISTEMP reconstructions of observations. Anomalies are calculated with respect to the 1979–2015 average for each data set. Shading shows the range of the annual global mean values over the four FRVOLC ensemble members, and red asterisks show the mean of the FRVOLC ensemble. Lines show 5 year running averages of the annual anomalies for simulations and observations. Least squares linear fit trends are listed.

gives confidence that the climate response of the model to long-term changes in greenhouse gases agrees with observations. Least squares linear fit trends for 1975–2016 are  $2.45 \pm 0.11$  K/century for the FRVOLC ensemble, which is slightly larger than those for HadCRUT4 ( $2.16 \pm 0.16$ ) and GISTEMP ( $1.92 \pm 0.12$ ).

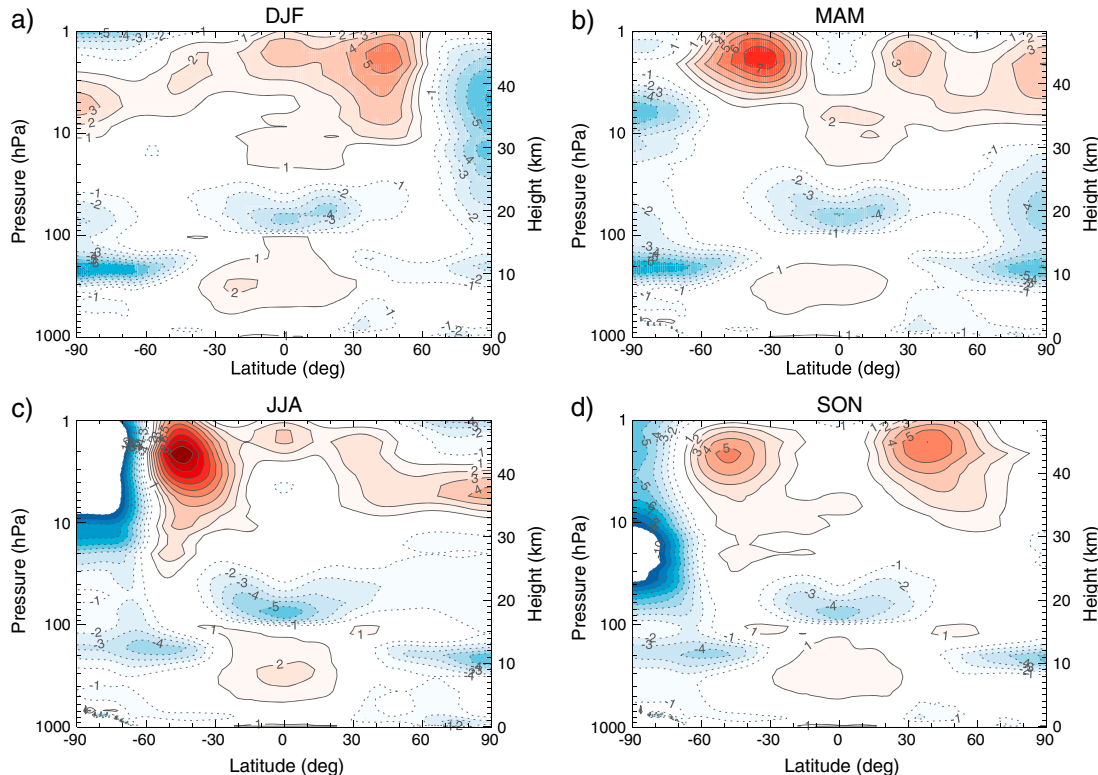


**Figure 2.** WACCM zonal mean temperature differences from ERA-Interim reanalysis for four seasons: (a) DJF, (b) MAM, (c) JJA, and (d) SON. Differences are plotted for the 1979–2014 time period from the FRVOLC ensemble average and the same years for ERA-Interim. The contour interval is 1 K.

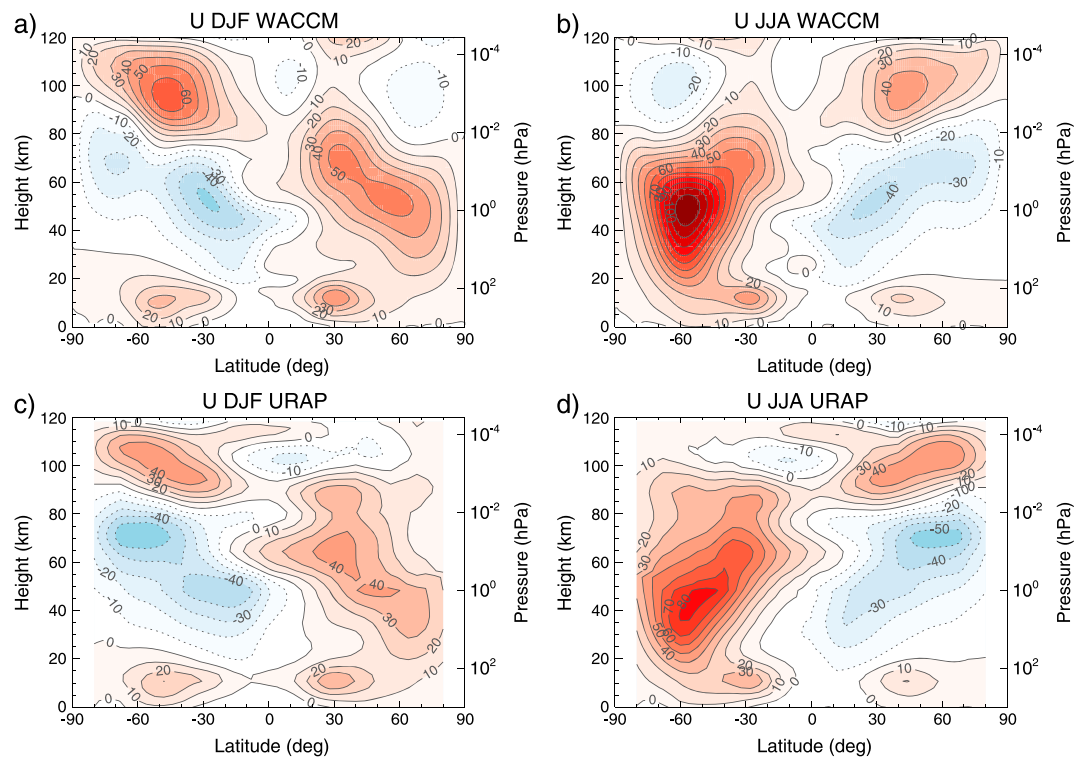


**Figure 3.** (a, b) WACCM and (c, d) URAP zonal mean wind for DJF (Figures 3a and 3c) and for JJA (Figures 3b and 3d). URAP and FRVOLC ensemble average winds are averaged over the years 1980–1999. The contour interval is  $10 \text{ m s}^{-1}$ .

WACCM has a very good representation of the mean temperature in the troposphere and middle atmosphere. As shown in Figure 2, throughout the entire troposphere the temperature bias relative to ERA-Interim reanalysis (ERA-Interim, Dee et al., 2011) is less than 2 K, with only the tropical midtroposphere carrying a bias greater than 1 K throughout the year (not shown). WACCM has a cold bias near the tropopause of  $-2$  to  $-4$  K in both the extratropics and the tropics throughout most of the year. This represents an improvement over CESM1(WACCM) (Marsh et al., 2013), which ran at  $1.9^\circ \text{ latitude} \times 2.5^\circ \text{ longitude}$  and exhibited extratropical biases ranging from  $-6$  to  $-8$  K. We attribute this improvement to the improved horizontal resolution. Charlton-Perez et al. (2013) showed that the CMIP5 multimodel average also carries a  $-4$  K bias in the extratropical tropopause temperatures.

Lower stratospheric (below 10 hPa) mean temperatures in WACCM are in good overall agreement with observations, as shown in Figure 2. In the upper stratosphere (1–10 hPa), WACCM has a warm bias ( $< 10$  K) between  $-60^\circ\text{S}$  and  $60^\circ\text{N}$  and a cold bias of up to 16 K at the winter pole. WACCM also has a cold bias ( $< 12$  K) in the south polar stratosphere in autumn (March-April-May, MAM) and spring (September-October-November, SON). These biases are of the same magnitude or smaller than those in CESM1(WACCM) (not shown, Marsh et al., 2013).

The summer mesopause in WACCM is near 87 km (log-pressure height) with temperature in January of 131 K (at  $80^\circ\text{S}$ ) and 130 K in July (at  $80^\circ\text{N}$ ). This is in reasonable agreement with Sounding of the Atmosphere using Broadband Emission Radiometry (SABER) observations (Xu et al., 2007) which show mesopause temperatures of 134 K in January (at  $80^\circ\text{S}$ ) and 127 K in July (at  $80^\circ\text{N}$ ). Zonal mean winds averaged over December-January-February (DJF) and June-July-August (JJA) for WACCM are shown in Figure 3 along with winds from the Upper Atmosphere Research Satellite Reference Atmosphere Project (URAP) climatology (Swinbank & Ortland, 2003). The overall DJF stratospheric and mesospheric wind structure is in good agreement with URAP. The model climatology is improved over CESM1(WACCM), with a few remaining biases. The stratospheric Northern Hemisphere (NH) jet in DJF is  $\sim 10 \text{ m s}^{-1}$  stronger than observed (associated with slightly colder than observed temperatures), and the summer stratospheric jet is too weak between  $60^\circ\text{S}$  and  $90^\circ\text{S}$  above

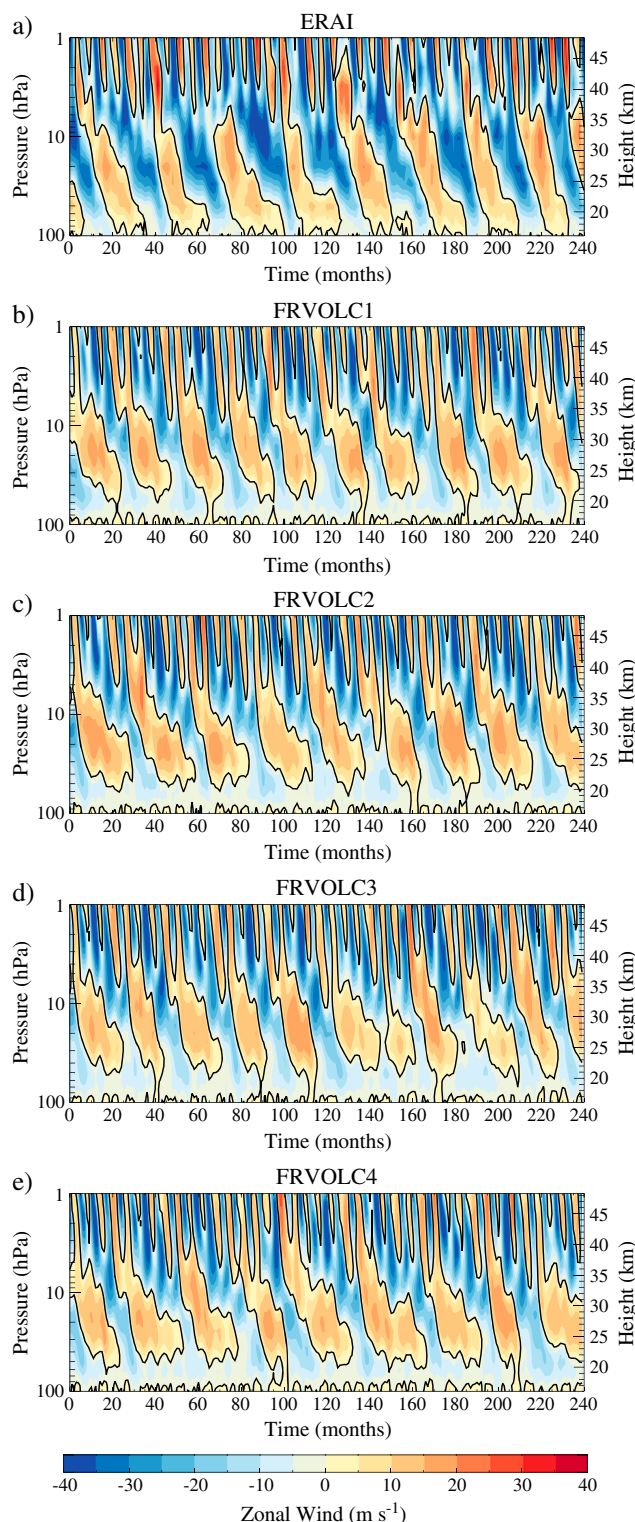


**Figure 4.** Tropical zonal winds ( $2^{\circ}\text{S}$ – $2^{\circ}\text{N}$ ) from 1980 to 2000 for (a) ERA-Interim reanalysis and (b–e) WACCM FRVOLC ensemble members. Contours are plotted in intervals of  $5 \text{ m s}^{-1}$ .

10 hPa. In JJA, the NH summer jet has very good agreement to URAP and is much improved between 0 and  $30^{\circ}\text{N}$  compared to WACCM3 and CESM1(WACCM), which carried a  $30 \text{ m s}^{-1}$  bias in this region (Marsh et al., 2013; Richter et al., 2010). The Southern Hemisphere stratospheric westerly jet is too strong in WACCM; however, unlike in WACCM3 and CESM1(WACCM) it is tilting in the correct direction (toward the equator as height increases).

### 3.2. QBO and Stratospheric Chemistry

WACCM has an internally generated QBO as shown in Figure 4. The period of the QBO in the FRVOLC ensemble varies between 19 and 36 months, with mean periods for each ensemble member varying from 23 to 27 months. In observations, the QBO period ranges between 20 and 34 months, with a mean of 28 months. The amplitude of the westerly QBO phase is between  $15$  and  $20 \text{ m s}^{-1}$ , exactly as in observations. The easterly QBO phase amplitude ranges between  $20$  and  $25 \text{ m s}^{-1}$  and is hence weaker than observed by  $10 \text{ m s}^{-1}$ . Further improvements to the representation of the QBO in WACCM require a substantial increase in the vertical resolution (Richter et al., 2014).

The stratospheric water vapor “tape recorder” (Mote et al., 1996) is well represented in WACCM, consistent with a good representation of tropical tropopause temperatures. A good representation of water vapor in the stratosphere is important for climate because of the role of water vapor as a greenhouse gas. Water vapor also strongly impacts stratospheric chemical cycles affecting ozone, which is an important radiatively active gas. In comparison to Aura MLS satellite observations (Livesey et al., 2016) between 2004 and 2014, the magnitude of both dry and wet phases of the tape recorder follows exactly the observed range (Figure 5). The slope of the tape recorder in the model is in good agreement with the observations, with a slightly stronger tropical upwelling in the lower stratosphere.

WACCM zonal mean stratospheric ozone column shows very good agreement with observations and excellent agreement in high latitudes (Figure 6). The representation of ozone in WACCM is improved over previous versions of WACCM. Figure 6 compares the zonal average stratospheric column ozone with a  $5^{\circ}$  latitude  $\times$   $10^{\circ}$  longitude gridded product, based on MLS and NASA Ozone Monitoring Instrument (OMI) observations, averaged between 2005 and 2010 (Ziemke et al., 2011). This figure shows agreement within 8% in high latitudes for four different seasons of the mean value of the FRVOLC ensemble with the observations. The observations generally lie within one standard deviation of ensemble variability at high latitudes, with the exception of  $60^{\circ}\text{S}$  in April. We attribute this improved performance to the improved horizontal resolution and dynamical improvements associated with modifications to the gravity wave parameterization (Garcia et al., 2017). The model underestimates column ozone in the tropics by 5–20%, which may be due to overly rapid transport.

### 3.3. Volcanic Aerosol Evolution

In order to validate that our model produces a reasonable response to stratospheric  $\text{SO}_2$  perturbations, we compare the period from 1 January 1990 to 1 January 2000 in our simulations to observations. This period includes the eruption of Mount Pinatubo on 15 June 1991,

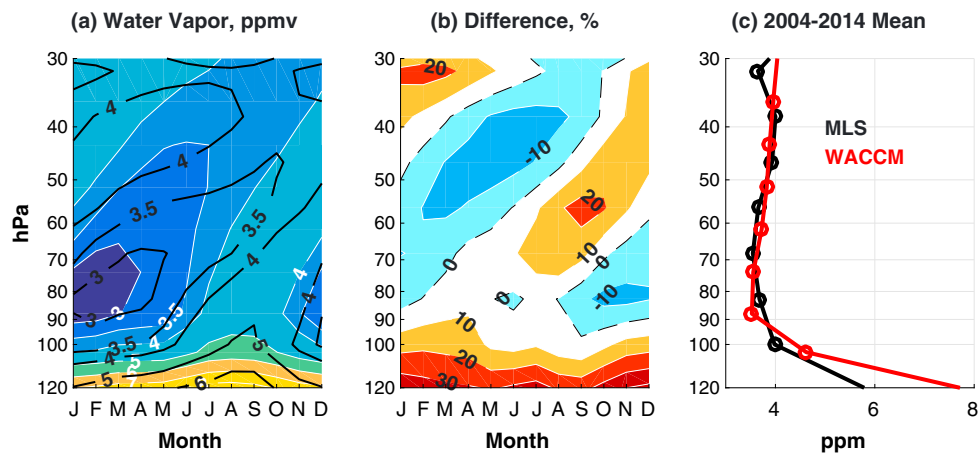


**Figure 5.** (a) Height-time seasonal variations of H<sub>2</sub>O mixing ratios (ppmv) averaged between latitudes 10°N–10°S and years 2004–2014 for (a) the WACCM FRVOLC ensemble average (color-filled white contours) and MLS satellite observations (black contours); (b) percent difference between the ensemble average and observations, 100 × (FRVOLC – MLS)/MLS; and (c) 2004–2014 mean vertical profiles of H<sub>2</sub>O mixing ratios (ppmv) from MLS (black) and FRVOLC (red).

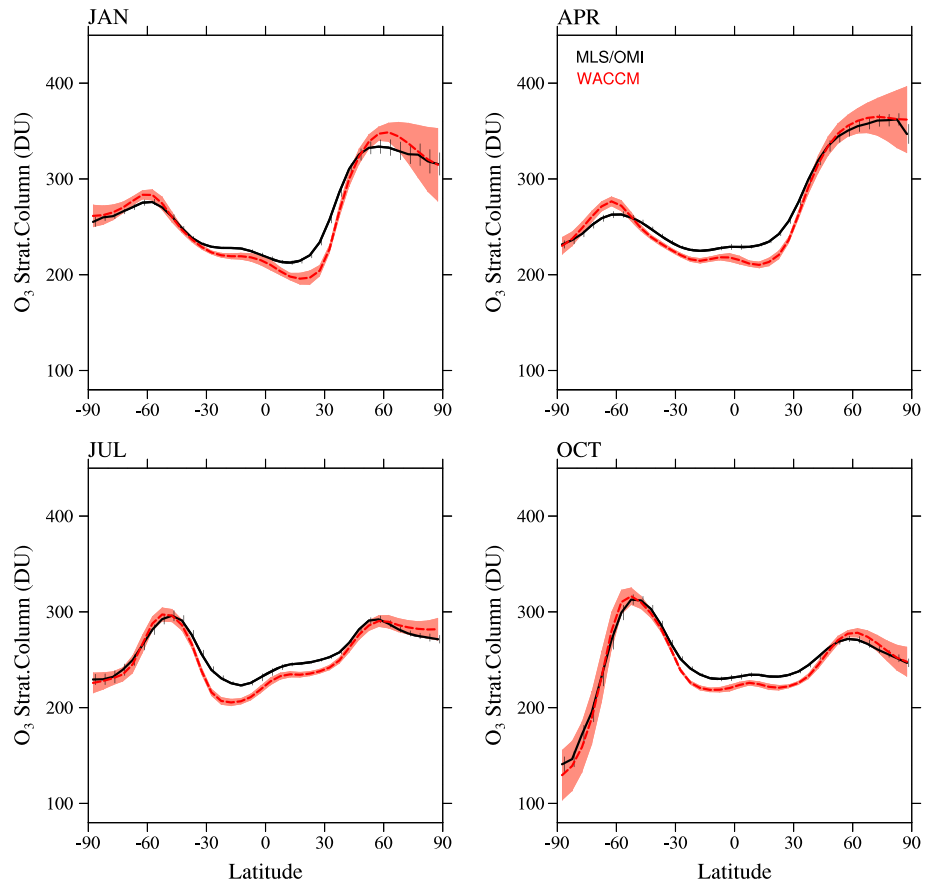


**Figure 6.** Monthly and zonally averaged stratospheric ozone column (in DU) comparison between OMI/MLS observations between 2004 and 2010 (black) and the WACCM FRVOLC ensemble (red) between 2004 and 2010 (for ozone <150 ppb in the model), for four months. OMI/MLS error bars show the zonally averaged 2 $\sigma$  6 year root-mean-square standard error of the mean at a given grid point, derived from the gridded product (Ziemke et al., 2011). Model results are interpolated to the same 5° latitude grid as the observations. Shading indicates the standard deviation (1 $\sigma$ ) of the interannual variability per latitude interval for the FRVOLC ensemble.

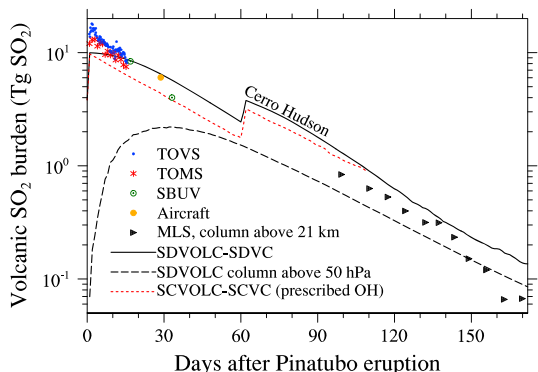


**Figure 7.** Calculated global volcanic SO<sub>2</sub> burden following the 15 June 1991 eruption of Mount Pinatubo is compared to observations. The solid line shows the daily average global burden of SO<sub>2</sub> calculated in the SDVOLC simulation minus the nonvolcanic SO<sub>2</sub> burden calculated in the SDVC simulation. The dashed red line shows the same for SCVOLC minus SCVC. The SO<sub>2</sub> burden is less than 10 Tg in the day 0 average because the eruption occurred midday. The additional input of 1.5 Tg SO<sub>2</sub> from the 12 August eruption of Cerro Hudson is noted 60 days after the Pinatubo eruption. Observations from TOVS (blue circles) and TOMS (red asterisks) show an initial burden of 13–18 Tg SO<sub>2</sub>, of which 10 Tg remained after loss to sedimenting ice and ash in the first 7–9 days (Guo, Bluth, et al., 2004). Observations from SBUV, aircraft, and MLS are shown as presented in Read et al. (1993). Because MLS column is integrated above 21 km, the WACCM column integrated above 50 hPa (dashed black line) is shown for comparison.

tions 7–9 days after the beginning of the eruption, when more than 99% of the ash and ice particles had been removed (Guo, Rose, et al., 2004). This “climatically relevant” sulfur input from Pinatubo is consistent with the 3.7 to 6.7 Tg peak sulfur content of stratospheric aerosol mass following the eruption derived from satellite observations from the High-resolution Infrared Radation Sounder (HIRS, Baran & Foot, 1994) and the Improved Stratospheric and Mesospheric Sounder (Lambert et al., 1993), as discussed in Dhomse et al. (2014). The evolution of aerosol mass burden calculated in WACCM following Pinatubo is consistent with HIRS observations, as shown in Figure 1 of Mills et al. (2016).

Additional SO<sub>2</sub> observations shown in Figure 7, from the Solar Backscatter Ultraviolet Radiometer-2 (SBUV/2), the Microwave Limb Sounder (MLS) aboard the Upper Atmosphere Research Satellite, and a high-resolution infrared spectrometer aboard an aircraft (Mankin et al., 1992) are presented as shown in Read et al. (1993). Our calculations show general agreement with these observations within their limitations. As indicated in Figure 7, the eruption of Cerro Hudson (45.9°S, 73.0°W) emitted 1.5 Tg SO<sub>2</sub> roughly 2 months after Pinatubo. This additional input was not observed by MLS, which integrated SO<sub>2</sub> above 21 km, well above the height of the Cerro Hudson plume. The dashed line shows the SO<sub>2</sub> burden in WACCM above 50 hPa, for comparison to the MLS observations.

Read et al. (1993) used these observations to derive a 33 day *e*-folding decay time with an extrapolated initial SO<sub>2</sub> injection of 17 Tg. Our calculations point to an interpretation of this apparent steady exponential decay as the superposition of two more variable processes: loss on ash and ice and oxidation by OH. We note that the slope of the semilogarithmic plot of SO<sub>2</sub> burden versus time shown for SDVOLC minus SDVC in Figure 7 indicates a much longer initial lifetime, decreasing to a constant slope by 30 days after the eruption. The reason for this is the rapid consumption of OH by SO<sub>2</sub> oxidation within the initial dense SO<sub>2</sub> cloud, which limits the availability of OH and hence the SO<sub>2</sub> oxidation rate. As Figure 8 shows, OH is reduced by more than 95% within the cloud as it is transported in the first weeks. Figure 9 shows the daily *e*-folding decay time of volcanic SO<sub>2</sub> as a function of days after the eruption. As the cloud disperses to larger volumes, OH recovers, and the initial *e*-folding decay time of more than 400 days drops over the first month to reach a constant value of  $30.9 \pm 0.5$  days (45 to 59 days after eruption). In contrast, the volcanic SO<sub>2</sub> in our SCVOLC simulation, for which OH is prescribed, decays with a constant *e*-folding time of  $34.1 \pm 1.4$  days (2 to 21 days after eruption, Figures 7 and 9). The specified chemistry simulations show greater variability, particularly as volcanic

which produced the best observed large (>10 Tg) injection of SO<sub>2</sub> into the stratosphere to date. Comparison of simulated surface climate response to the volcanic eruption based on observations is complicated by climate variability, including a coincident El Niño event that tended to counteract the reduction in global average temperatures following the eruption, as well as other underlying climate oscillations (e.g., Carty et al., 2013). We therefore constrain our calculations by using SD-WACCM, which incorporates a data ocean model with observed sea surface temperatures, as well as nudged atmospheric temperatures and winds.

The first step in the production of sulfate aerosol from stratospheric SO<sub>2</sub> input is chemical oxidation by the OH radical, which, via intermediate steps, produces H<sub>2</sub>SO<sub>4</sub> gas. Figure 7 shows the time evolution of the total burden of volcanic (SDVOLC minus SDVC) SO<sub>2</sub> in WACCM, compared to observations of the stratospheric burden following the eruption. Guo, Bluth, et al. (2004) present and evaluate the SO<sub>2</sub> observations from the Total Ozone Mapping Spectrometer (TOMS) and the Television Infrared Observation Satellite Optical Vertical Sounder (TOVS) in the first 15 days after the Pinatubo eruption. That work suggested that much of the initial 14 to 23 Tg of SO<sub>2</sub> (7 to 11.5 Tg of sulfur) from Pinatubo was rapidly catalyzed on ash and ice, fast processes that are not currently included in WACCM. As in Mills et al. (2016), we input 10.0 Tg of SO<sub>2</sub> (5.0 Tg of sulfur) from Pinatubo in WACCM on the day of the eruption, matching the burden from TOMS and TOVS observa-

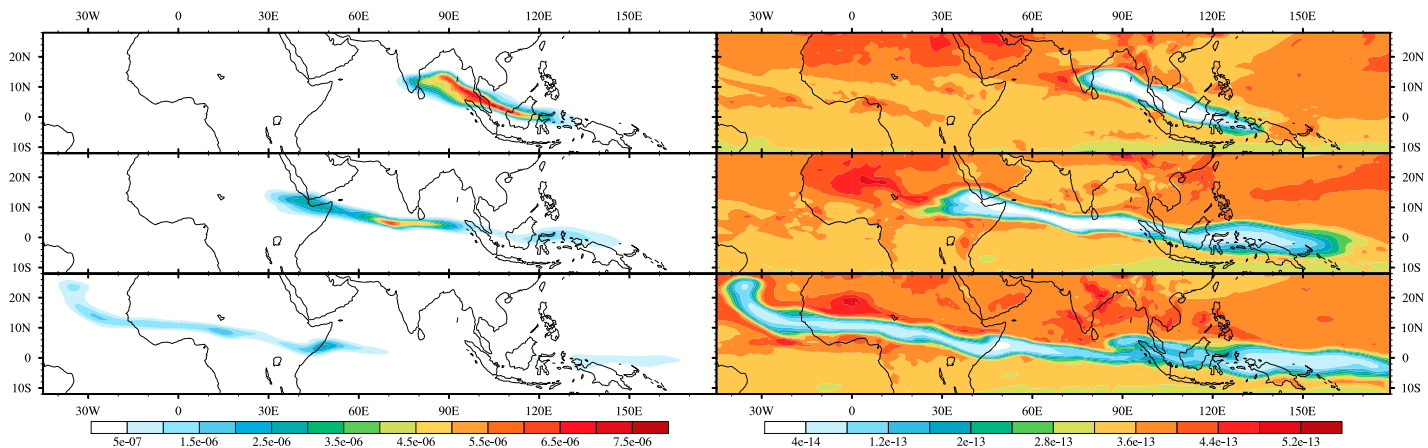


**Figure 8.** Maps of calculated daily averaged (left column)  $\text{SO}_2$  and (right column)  $\text{OH}$  volume mixing ratios (moles/mole air) at 61 hPa on (top row) days 3, (middle row) 7, and (bottom row) 13 after the 15 June 1991 eruption of Mount Pinatubo. Calculations are shown from the SDVOLC simulation.

minus clean  $\text{SO}_2$  burdens approach zero, because they are not nudged as the SD simulations are and therefore have unmatched nonvolcanic burdens.

Constant  $e$ -folding decay times ranging from 23 to 35 days have been derived from observations for Pinatubo  $\text{SO}_2$  (Bluth et al., 1992; Guo, Bluth, et al., 2004; McPeters, 1993; Read et al., 1993). These constant  $e$ -folding times do not distinguish the rapid initial removal of  $\text{SO}_2$  on sedimenting ash and ice in the initial days after the eruption from the variable chemical oxidation rate due to  $\text{OH}$  depletion. Our simulations with interactive  $\text{OH}$  chemistry find a similar constant terminal  $e$ -folding time, but we also find the “average initial  $e$ -folding time” for oxidation to be 47 days, calculated as the time for the initial 10 Tg of Pinatubo  $\text{SO}_2$  to be reduced by  $1/e$  to 3.7 Tg. Pinto et al. (1989) examined the effects of large stratospheric  $\text{SO}_2$  injections on the  $e$ -folding time for loss of  $\text{SO}_2$  by  $\text{OH}$ . Using a one-dimensional model that accounted for the horizontal dispersion and expansion of volcanic  $\text{SO}_2$  clouds, they calculated that an injection of 10 Tg of  $\text{SO}_2$  should increase the  $e$ -folding time from 1.3 to 1.8 months, which is consistent with our calculations. Bekki (1995) found the reduction in  $\text{OH}$  oxidation to be significant for a much larger 200 Tg injection but concluded that the effects of Pinatubo’s  $\sim$ 20 Tg  $\text{SO}_2$  injection on  $\text{OH}$  “would have been too modest to have had a noticeable effect on

the global  $\text{SO}_2$  removal rate.” That assessment, however, relied on a coarse zonally averaged two-dimensional model with very large grid cells ( $\sim 10^\circ$  latitude  $\times 360^\circ$  longitude), which could not account for the local  $\text{OH}$  depletion within the  $\text{SO}_2$  cloud in three spatial dimensions.

Several studies examined the effects of dense  $\text{SO}_2$  clouds and volcanic aerosols on  $\text{OH}$  levels due to absorption and scattering of sunlight, which affects photolysis rates (Bândă et al., 2015; Bekki, 1995; Pinto et al., 1989; Pitari, Cionni, et al., 2016). WACCM does not include such effects on photolysis rates, which these studies indicate are of lesser significance than reductions in  $\text{OH}$  due to sulfur chemistry. Bândă et al. (2015) found no significant effect of  $\text{SO}_2$  absorption on the  $e$ -folding time of  $\text{SO}_2$  from the 1991 Pinatubo eruption. Impacts of stratospheric sulfate geoengineering on photolysis rates and the oxidation capacity of the troposphere might be more significant (Pitari et al., 2014; Visoni et al., 2017). Our studies with WACCM focus on middle atmosphere chemistry, which would be less affected by such effects than the troposphere.

Our results imply that interactive  $\text{OH}$  chemistry is essential to accurately calculating oxidation and dispersal following the input of 10 Tg or more of  $\text{SO}_2$  into the stratosphere. Studies of interactive stratospheric aerosols

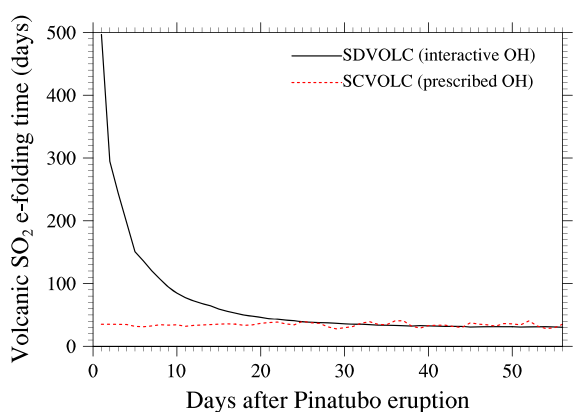


**Figure 9.** Volcanic  $\text{SO}_2$   $e$ -folding time (days) shown as a function of days following the 15 June 1991 eruption of Mount Pinatubo in the SCVOLC (solid black line) and SCVOLC (dashed red line) simulations. The  $e$ -folding time is derived from the daily change in the global volcanic  $\text{SO}_2$  burden. Volcanic  $\text{SO}_2$  is calculated by subtracting the global burdens from volcanically clean simulations (SDVC and SCVC, respectively).

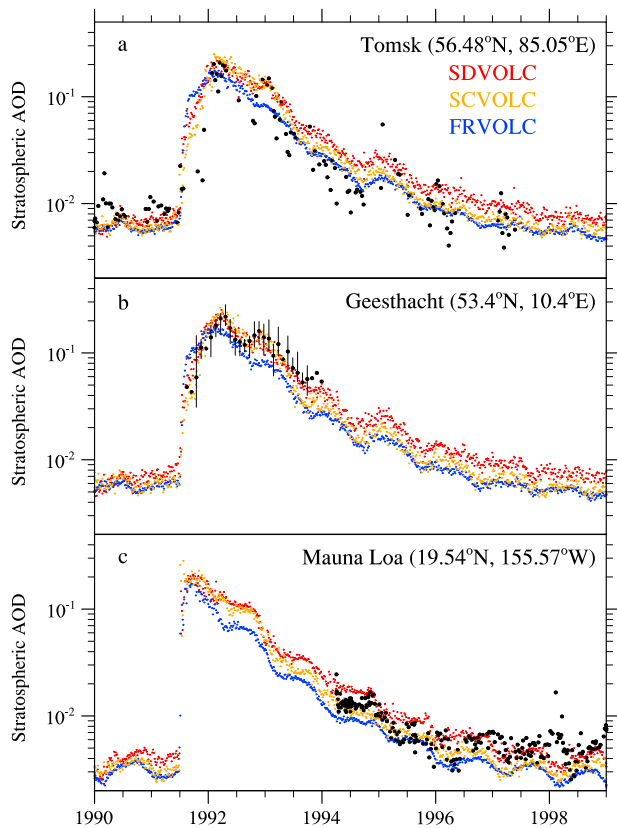


**Figure 10.** Aerosol optical depth (AOD) measured by lidars at three locations (black circles) are compared to calculated 5 day average AOD above the tropopause in corresponding model columns from our SDVOLC (red dots), FRVOLC (ensemble average, blue dots), and SCVOLC (orange dots) simulations. Observations are (a) integrated backscatter from 15–30 km measured in Tomsk, Siberia (Zuev et al., 2016), converted to AOD using a lidar ratio of 50; (b) AOD above the tropopause measured in Geesthacht, Germany (Ansmann et al., 1997); and (c) AOD above the tropopause measured in Mauna Loa, Hawaii (Hofmann et al., 2009; Ridley et al., 2014).

depth (SAOD) at 550 nm for 1990–1998 measured by lidars at three locations (black circles) to 5 day average values calculated at the same locations in our SDVOLC (red dots), FRVOLC (blue dots, ensemble average), and SCVOLC (orange dots) simulations. The reduced SAOD in the FRVOLC ensemble compared to SDVOLC reflects a lower stratospheric aerosol burden and a shorter aerosol lifetime. This relates to faster circulation and higher (~0.5 km) tropical tropopause altitudes in FR-WACCM. It also relates to the phase of the QBO at the time of the eruption, which agrees with observations in SDVOLC (easterlies above 26 km overlying westerlies below) but which is variable in the FRVOLC ensemble. The easterly shear in SDVOLC is associated with lofting of the Pinatubo aerosols in the tropics, while the westerly shear is associated with descent and transport to higher latitudes (Trepte & Hitchman, 1992), which we see in our simulations. This difference illustrates a mode of variability affecting volcanic aerosol evolution in the atmosphere compared to models with interactive QBOs. Comparison of SAOD in SCVOLC to FRVOLC shows the impact of the enhanced self-lofting of Pinatubo aerosols when OH depletion is not accounted for.

Figure 10a compares to a newly available lidar record from Tomsk, Siberia (Zuev et al., 2016). While the tropopause altitude is generally 11–13 km, the lidar backscatter was integrated between 15 and 30 km. We have converted the integrated backscatter to aerosol optical depth (AOD) using a lidar ratio (integrated extinction/backscatter) of 50, which has been found to be appropriate for the stratosphere within 20% (Jäger & Deshler, 2002, 2003; Ridley et al., 2014). Our calculated AOD is integrated above the tropopause, yielding slightly higher values in SDVOLC over the Pinatubo period than the integrated backscatter, which

in models that use invariant prescribed OH values calculated constant e-folding times for Pinatubo SO<sub>2</sub> of 29–33 days (Aquila et al., 2012; Niemeier et al., 2009), leading to faster initial oxidation. Bekki and Pyle (1994) used a two-dimensional model that neglected feedbacks between SO<sub>2</sub> photochemistry and other chemical species and calculated a longer e-folding time of 40 days, which they account for by stating “Since SO<sub>2</sub> is only significantly removed by OH, this small difference is probably because the modeled OH levels are low compared to reality in the region of the volcanic cloud.” Sekiya et al. (2016) calculated an e-folding time of 38–40 days, using a general circulation model with interactive OH.

The University of L’Aquila Composition-Climate Coupled Model (ULAQ-CCM), which also includes interactive OH, found a 31 day e-folding time for a 20 Tg SO<sub>2</sub> Pinatubo eruption based on exponential decay between days 45 and 165 after the eruption but did not report on variations within the first month (Pitari, Di Genova, et al., 2016). They also found a much shorter 18 day e-folding time for a much smaller 1.2 Tg SO<sub>2</sub> eruption, which they account to “more abundant OH due to an inefficient sink by sulfur dioxide” in the smaller volcanic cloud. The 19 day and 43 day e-folding times that they find for eruptions of 7 and 12 Tg SO<sub>2</sub>, respectively, suggest that factors other than the mass of SO<sub>2</sub> erupted also affected their calculations.

Inclusion of interactive OH chemistry in WACCM is key to understanding variable oxidation and its importance for the subsequent size and latitudinal distribution of stratospheric aerosol. We found significantly greater self-lofting of volcanic aerosol in our SCVOLC simulation than in the FRVOLC ensemble for the two largest eruptions simulated (El Chichón 1982 and Pinatubo 1991). This is due to radiative interaction with the dense aerosol clouds that result from rapid oxidation of the volcanic SO<sub>2</sub> before it disperses (not shown).

Mills et al. (2016) presented validations of volcanic aerosol properties in WACCM with CAM5 physics, using half the horizontal resolution used in this study. Here we present similar validations before examining radiative impacts. In Figure 10, we compare stratospheric aerosol optical

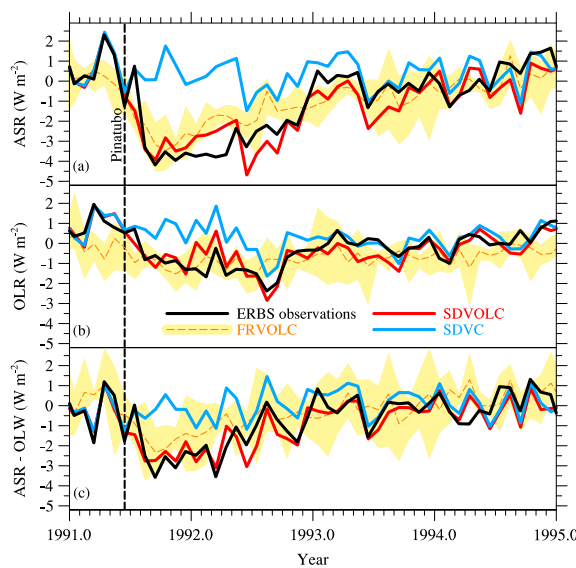


**Figure 11.** Top-of-model all-sky radiative fluxes from our SDVOLC (solid red) and SDVC (solid blue) simulations are compared to top-of-atmosphere ERBS observations (black) merged with additional data to provide a global data set (Allan et al., 2014; Liu et al., 2015). Monthly mean net fluxes are shown for January 1991 to December 1995, normalized and deseasonalized by subtracting the corresponding flux for each month from 1999, a volcanically quiescent year. Fluxes from our FRVOLC ensemble average (dashed orange line) and range (yellow shading) are also shown. (a) Absorbed solar radiation (positive for downward fluxes); (b) outgoing longwave radiation (positive for upward fluxes); and (c) net radiative flux (positive for downward fluxes).

The SDVC simulation includes the latter effect, as it is nudged and driven by observed tropospheric and sea surface temperatures, which include this cooling. This cooling reduces OLR by up to  $1.5\text{--}2.0\text{ W m}^{-2}$  by August 1992. Inclusion of volcanic aerosols in our SDVOLC simulation, however, is necessary to match the observed reduction of  $2.5\text{--}3.0\text{ W m}^{-2}$ . The differences in the OLR between the SDVC and SDVOLC simulations are due to aerosol longwave absorption, secondary effects of aerosols on clouds, and cooling of land surface temperatures.

Figure 11c shows net radiative flux (ASR-OLR, positive for downward fluxes), a measure of the radiative energy imbalance forcing the Earth's climate. The SDVC case shows natural variability, with a slight upward trend due to increases in greenhouse gases. The SDVOLC shows a drop in the net flux following the Pinatubo eruption which generally matches well the observations. The FRVOLC ensemble shows a similar average reduction and significant variability. In general, the radiative response to Pinatubo in WACCM is a significant improvement over previous models using prescribed volcanic forcing (Driscoll et al., 2012; Neely et al., 2016). This is due to both the limitations of prescribed stratospheric aerosol climatologies derived from satellite observations (Mills et al., 2016; Ridley et al., 2014) and the neglect of aerosol-cloud interactions.

The efficacy of volcanic forcing in climate models is quantified by normalizing changes in all-sky net radiative fluxes to changes in SAOD. The Fifth Assessment Report of the Intergovernmental Panel on Climate Change (Myhre et al., 2013) uses the value of  $-25\text{ W m}^{-2}$  per unit change in volcanic SAOD, based on fixed sea surface temperature simulations of the Pinatubo eruption in GISS Model E with prescribed stratospheric aerosol (Hansen et al., 2005). ULAQ-CCM, with prognostic volcanic aerosols, calculates volcanic forcing efficiencies for Pinatubo of  $-15.3\text{ W m}^{-2}\text{ SAOD}^{-1}$  in all-sky conditions (Pitari, Di Genova, et al., 2016). We calculate the efficacy of Pinatubo volcanic forcing in WACCM by linearly regressing the differences between volcanic and clean simulations in annually averaged top-of-model all-sky net fluxes and global SAOD for the years 1991–1996. For SDVOLC minus SDVC, we calculate  $-18.3 \pm 1.0\text{ W m}^{-2}\text{ SAOD}^{-1}$ . This indicates a reduced volcanic radiative forcing efficacy in WACCM compared to Hansen et al. (2005), which neglected the interaction of volcanic aerosol with clouds, and a greater efficacy compared to Pitari, Di Genova, et al. (2016). For SCVOLC

excludes the lowermost 2–4 km. As in Mills et al. (2016), our SDVOLC calculations show excellent agreement over the Pinatubo period with the lidars at Geestacht, Germany (Ansmann et al., 1997) (Figure 10b), and Mauna Loa, Hawaii (Hofmann et al., 2009; Ridley et al., 2014) (Figure 10c), both of which are integrated above the tropopause.

### 3.4. Volcanic Aerosol Radiative Forcing

In Figure 11, we show global mean all-sky net radiative fluxes at the top of the model, compared to the observed global mean time series from the merged ERBS data (Allan et al., 2014; Liu et al., 2015). Monthly mean net fluxes are shown for January 1991 to December 1995, normalized and deseasonalized by subtracting the corresponding flux for each month from 1999, a volcanically quiescent year. Figure 11a shows the deseasonalized anomaly in the absorbed solar radiation (ASR, positive for downward fluxes), measured as incident minus reflected shortwave radiation. Following the Pinatubo eruption, observations show a dramatic reduction in ASR, due to increased scattering of sunlight to space from volcanic aerosols, not fully recovering until mid-1994. Our SDVOLC simulation calculates a remarkably similar reduction and recovery in ASR. The FRVOLC ensemble average shows a similar reduction in ASR, and the ensemble range shows the role of other unconstrained climate variables, including ocean states. The SDVC simulation reveals the effects of constrained sea surface and atmospheric temperatures on ASR variability without volcanic forcing.

Figure 11b shows the deseasonalized anomaly in the outgoing longwave radiation (OLR, positive for upward fluxes). Pinatubo aerosols reduced OLR both by direct absorption of longwave radiation and by reducing temperatures in the troposphere and at the Earth's surface.

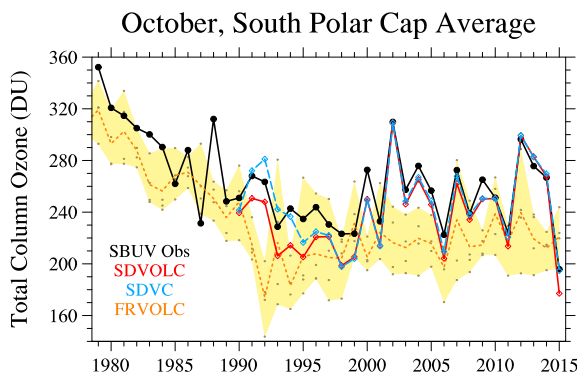


**Figure 12.** October monthly average column ozone over the south polar cap ( $63\text{--}90^\circ\text{S}$ ) for years 1980–2016 from SBUV satellite observations (black solid line and circles) and in WACCM SDVOLC (red solid line and diamonds), SDVC (blue dashed line and diamonds), and FRVOLC experiments. The orange dashed line shows the ensemble average, and yellow shading shows the ensemble range. Grey dots show monthly averages for individual FRVOLC ensemble members.

satellite instruments (McPeters et al., 2013). The observations show the development of the ozone hole in the 1980s, with significant interannual variability depending on temperature and volcanic aerosol loading following the eruptions of El Chichón (1982) and Pinatubo (1991). The FRVOLC ensemble reproduces the magnitude of the decline in Antarctic ozone in October from 1980 to the mid-1990s and indicates significant drops following these two major tropical eruptions. Ozone loss leveled off after a peak in the late 1990s, and FRVOLC reproduces this general trend in the observations, although ozone columns are generally biased low throughout this simulation, consistent with the cold bias in the Antarctic spring stratosphere (see Figure 2).

Comparison of the SDVOLC and SDVC simulations, which were both initialized from FRVOLC on 1 January 1990, shows  $\sim 40$  DU of polar cap ozone loss attributable to the 1991 eruptions of Pinatubo and Cerro Hudson. Both SD simulations match the interannual variability in Antarctic ozone particularly well in the period of reduced and moderate volcanic aerosols post-2000. Significant drops in ozone followed the eruptions of Puyehue-Cordón Caulle (2011,  $40.6^\circ\text{S}$ ,  $72.1^\circ\text{W}$ ) and Calbuco (2015,  $41.3^\circ\text{S}$ ,  $72.6^\circ\text{W}$ ). While comparison of SDVOLC to SDVC in 2011 and 2015 shows significant effects due to volcanic aerosols, cold temperatures also played a role, as revealed by significant drops in the SDVC ozone columns in those years. Because ozone heats the stratosphere, cold stratospheric temperatures are a positive feedback of polar ozone loss, and thermal and dynamical feedbacks may enhance the loss of polar ozone following volcanic eruptions (Ivy et al., 2017; Pitari, Cionni, et al., 2016; Solomon et al., 2016).

#### 4. Conclusions

We have described a new version of WACCM with improved horizontal resolution, updated physics, and an interactive QBO. We have validated the chemistry and climate of WACCM with detailed comparisons to observations. We have paid particular attention to the evolution and impacts of volcanic sulfate aerosol, which WACCM derives from emissions of  $\text{SO}_2$  gas. The completeness of the chemistry, dynamics, and aerosol microphysics qualify WACCM for studies of stratospheric sulfate geoengineering.

Our calculations reveal the importance of interactive chemistry to the development of sulfate aerosol from large inputs of  $\text{SO}_2$ . Previous findings of a  $\sim 30$  day e-folding decay time of  $\text{SO}_2$  from the 1991 eruption of Mount Pinatubo were based on observations that ignored the rapid initial losses of  $\text{SO}_2$  on ice and ash and on calculations that either did not include interactive OH chemistry or did not discuss the impacts of OH depletion in the first month after the eruption. We show that the dense  $\text{SO}_2$  cloud oxidized much more slowly in the first 2 weeks after the eruption due to the depletion of OH by the  $\text{SO}_2$  oxidation itself. We calculate a 47 day average initial e-folding decay time for the Pinatubo  $\text{SO}_2$  that remained aloft after the initial losses on ice and ash and show the calculated evolution of Pinatubo  $\text{SO}_2$  to be largely consistent

minus SCVC, we calculate  $-20.2 \pm 4.6 \text{ W m}^{-2} \text{ SAOD}^{-1}$ , suggesting that interactive chemistry is not a significant factor in volcanic radiative forcing efficacy in WACCM.

#### 3.5. Volcanic Impacts on Stratospheric Ozone

The Antarctic ozone hole, defined as a region where total column ozone measures less than 220 Dobson units (DU), has developed each austral spring since the early 1980s. The area of the ozone hole is at its largest in October, when total column ozone over Antarctica reaches minimum annual values. These minimum values depend on the amount of halogen loading in the stratosphere, as well as meteorology, with greater ozone loss in colder years. In addition, ozone loss increases when enhanced sulfate aerosol levels from volcanic eruptions reach the Antarctic stratosphere, due to the effects of heterogeneous chemistry on halogens (Portmann et al., 1996; Solomon et al., 2016).

Figure 12 shows observations of total column ozone measured from the Solar Backscatter Ultraviolet satellite (SBUV), averaged over  $63\text{--}90^\circ\text{S}$ , from 1980 to 2015. The SBUV record has been carefully calibrated and compared to observations from ground-based, in situ, and other

with observations. The evolution of stratospheric AOD following the Pinatubo eruption in WACCM agrees well with lidar observations from three independent locations at midlatitudes and in the tropics. The radiative impacts of Pinatubo on ASR and OLR match satellite observations very well. This is crucial for assessing the impacts of stratospheric  $\text{SO}_2$  injections on surface climate and on stratospheric chemistry and dynamics.

We have validated the climate and chemistry in an ensemble of fully coupled WACCM simulation of the years 1975–2016. The trend in global average surface temperatures over this period closely matches that derived from observations. Temperatures and winds from the troposphere through the middle atmosphere agree well with observations. WACCM now includes an internally generated QBO, which exhibits a period close to that observed. This feature is important to studies of stratospheric sulfate geoengineering, which has been shown in other studies to disrupt the QBO. Stratospheric water vapor in WACCM is close to that observed, as is the seasonal cycle in water vapor mixing ratios entering from the troposphere. Stratospheric ozone columns in WACCM agree well with global satellite observations and with ground-based observations in Antarctica showing the development of the ozone hole over this period.

#### Acknowledgments

We thank Vladislav Gerasimov and Vladimir V. Zuev for providing lidar data from Tomsk. Mauna Loa lidar data were provided by NOAA ESRL Global Monitoring Division, Boulder, Colorado, USA (<http://esrl.noaa.gov/gmd/>). We thank Richard Allan for providing the merged ERBS data. We thank Diane Ivy for providing the polar cap average SBUV data. We thank Anne Smith, Dan Marsh, and three anonymous reviewers for providing many helpful comments on this manuscript. This research was developed with funding from the Defense Advanced Research Projects Agency (DARPA). The views, opinions, and/or findings expressed are those of the authors and should not be interpreted as representing the official views or policies of the Department of Defense or the U.S. Government. We acknowledge high-performance computing support from Yellowstone (ark:/85065/d7wd3xhc) provided by NCAR's Computational and Information Systems Laboratory, sponsored by the National Science Foundation. The CESM project is supported by the National Science Foundation (NSF) and the Office of Science (BER) of the U. S. Department of Energy (DOE). The National Center for Atmospheric Research is funded by the NSF. The Pacific Northwest National Laboratory is operated for the U.S. DOE by Battelle Memorial Institute under contract DE-AC05-76RL01830. The output of all model simulations discussed in this study are available at the NCAR Earth System Grid at doi:10.5065/D6PC313T. Data presented in this work, including the source code used for these simulations, may be obtained from M. J. M. (email: mmills@ucar.edu).

#### References

Albani, S., Mahowald, N. M., Perry, A. T., Scanza, R. A., Zender, C., Heavens, N. G., ... Otto-Bliesner, B. L. (2014). Improved dust representation in the Community Atmosphere Model. *Journal of Advances in Modeling Earth Systems*, 6(3), 541–570. <https://doi.org/10.1002/2013MS000279>

Allan, R. P., Liu, C., Loeb, N. G., Palmer, M. D., Roberts, M., Smith, D., & Vidale, P. L. (2014). Changes in global net radiative imbalance 1985–2012. *Geophysical Research Letters*, 41(15), 5588–5597. <https://doi.org/10.1002/2014GL060962>

Ansmann, A., Mattis, I., Wandinger, U., Wagner, F., Reichardt, J., & Deshler, T. (1997). Evolution of the Pinatubo aerosol: Raman lidar observations of particle optical depth, effective radius, mass, and surface area over Central Europe at 53.4°N. *Journal of the Atmospheric Sciences*, 54(22), 2630–2641. [https://doi.org/10.1175/1520-0469\(1997\)054%3C2630:EOTPAR%3E2.0.CO;2](https://doi.org/10.1175/1520-0469(1997)054%3C2630:EOTPAR%3E2.0.CO;2)

Aquila, V., Garfinkel, C. I., Newman, P. A., Oman, L. D., & Waugh, D. W. (2014). Modifications of the quasi-biennial oscillation by a geoengineering perturbation of the stratospheric aerosol layer. *Geophysical Research Letters*, 41(5), 1738–1744. <https://doi.org/10.1002/2013GL058818>

Aquila, V., Oman, L. D., Stolarski, R. S., Colarco, P. R., & Newman, P. A. (2012). Dispersion of the volcanic sulfate cloud from a Mount Pinatubo-like eruption. *Journal of Geophysical Research*, 117, D06216. <https://doi.org/10.1029/2011JD016968>

Bändä, N., Krol, M., Noije, T., Weele, M., Williams, J. E., Sager, P. L., ... Röckmann, T. (2015). The effect of stratospheric sulfur from Mount Pinatubo on tropospheric oxidizing capacity and methane. *Journal of Geophysical Research: Atmospheres*, 120, 1202–1220. <https://doi.org/10.1002/2014JD022137>

Baran, A. J., & Foot, J. S. (1994). New application of the operational sounder HIRS in determining a climatology of sulphuric acid aerosol from the Pinatubo eruption. *Journal of Geophysical Research*, 99(D12), 25673. <https://doi.org/10.1029/94JD02044>

Bekki, S. (1995). Oxidation of volcanic  $\text{SO}_2$ : A sink for stratospheric OH and  $\text{H}_2\text{O}$ . *Geophysical Research Letters*, 22(8), 913–916. <https://doi.org/10.1029/95GL00534>

Bekki, S., & Pyle, J. A. (1994). A two-dimensional modeling study of the volcanic eruption of Mount Pinatubo. *Journal of Geophysical Research*, 99(D9), 18,861–18,869. <https://doi.org/10.1029/94JD00667>

Bender, F. A. M., Ekman, A. M. L., & Rodhe, H. (2010). Response to the eruption of Mount Pinatubo in relation to climate sensitivity in the CMIP3 models. *Climate Dynamics*, 35(5), 875–886. <https://doi.org/10.1007/s00382-010-0777-3>

Bluth, G. J. S., Doiron, S. D., Schnetzler, C. C., Krueger, A. J., & Walter, L. S. (1992). Global tracking of the  $\text{SO}_2$  clouds from the June, 1991 Mount Pinatubo eruptions. *Geophysical Research Letters*, 19(2), 151–154. <https://doi.org/10.1029/91GL02792>

Budyko, M. I. (1977). *Climatic changes* (p. 244). Washington, DC: American Geophysical Union. <https://doi.org/10.1029/sp010>

Canty, T., Mascioli, N. R., Smarte, M. D., & Salawitch, R. J. (2013). An empirical model of global climate—Part 1: A critical evaluation of volcanic cooling. *Atmospheric Chemistry and Physics*, 13(8), 3997–4031. <https://doi.org/10.5194/acp-13-3997-2013>

Charlton-Perez, A. J., Baldwin, M. P., Birner, T., Black, R. X., Butler, A. H., Calvo, N., ... Watanabe, S. (2013). On the lack of stratospheric dynamical variability in low-top versions of the CMIP5 models. *Journal of Geophysical Research: Atmospheres*, 118, 2494–2505. <https://doi.org/10.1002/jgrd.50125>

Computational and Information Systems Laboratory (2012). *Yellowstone: IBM iDataPlex System (NCAR Strategic Capability Projects)*. Boulder, CO: National Center for Atmospheric Research. <http://n2t.net/ark:/85065/d7wd3xhc>

Cowtan, K., & Way, R. G. (2014). Coverage bias in the HadCRUT4 temperature series and its impact on recent temperature trends. *Quarterly Journal of the Royal Meteorological Society*, 140(683), 1935–1944. <https://doi.org/10.1002/qj.2297>

Crutzen, P. J. (2006). Albedo enhancement by stratospheric sulfur injections: A contribution to resolve a policy dilemma? *Climatic Change*, 77(3–4), 211–220. <https://doi.org/10.1007/s10584-006-9101-y>

Danabasoglu, G., Bates, S. C., Briegleb, B. P., Jayne, S. R., Jochum, M., Large, W. G., ... Yeager, S. G. (2012). The CCSM4 ocean component. *Journal of Climate*, 25(5), 1361–1389. <https://doi.org/10.1175/JCLI-D-11-00091.1>

Dee, D. P., Uppala, S., Simmons, A., Berrisford, P., Poli, P., Kobayashi, S., ... Vitart, F. (2011). The ERA-Interim reanalysis: Configuration and performance of the data assimilation system. *Quarterly Journal of the Royal Meteorological Society*, 137(656), 553–597. <https://doi.org/10.1002/qj.828>

Dhomse, S. S., Emmerson, K. M., Mann, G. W., Bellouin, N., Carslaw, K. S., Chipperfield, M. P., ... Thomason, L. W. (2014). Aerosol microphysics simulations of the Mt. Pinatubo eruption with the UM-UKCA composition-climate model. *Atmospheric Chemistry and Physics*, 14(20), 11,221–11,246. <https://doi.org/10.5194/acp-14-11221-2014>

Driscoll, S., Bozzo, A., Gray, L. J., Robock, A., & Stenchikov, G. (2012). Coupled Model Intercomparison Project 5 (CMIP5) simulations of climate following volcanic eruptions. *Journal of Geophysical Research*, 117, D17105. <https://doi.org/10.1029/2012JD017607>

English, J. M., Toon, O. B., & Mills, M. J. (2013). Microphysical simulations of large volcanic eruptions: Pinatubo and Toba. *Journal of Geophysical Research: Atmospheres*, 118, 1880–1895. <https://doi.org/10.1002/jgrd.50196>

Eyring, V., Bony, S., Meehl, G. A., Senior, C. A., Senior, C., Stevens, B., ... Taylor, K. E. (2016). Overview of the Coupled Model Intercomparison Project Phase 6 (CMIP6) experimental design and organization. *Geoscientific Model Development*, 9(5), 1937–1958. <https://doi.org/10.5194/gmd-9-1937-2016>

Garcia, R. R., Smith, A. K., Kinnison, D. E., de la Cámara, Á., & Murphy, D. J. (2017). Modification of the gravity wave parameterization in the Whole Atmosphere Community Climate Model: Motivation and results. *Journal of the Atmospheric Sciences*, 74(1), 275–291. <https://doi.org/10.1175/JAS-D-16-0104.1>

Gettelman, A., & Morrison, H. (2015). Advanced two-moment bulk microphysics for global models. Part I: Off-line tests and comparison with other schemes. *Journal of Climate*, 28(3), 1268–1287. <https://doi.org/10.1175/JCLI-D-14-00102.1>

GISTEMP Team (2017). GISS Surface Temperature Analysis (GISTEMP), NASA Goddard Institute for Space Studies. Retrieved from <https://data.giss.nasa.gov/gistemp/>, (Accessed 13 February 2017).

Guenther, A. B., Jiang, X., Heald, C. L., Sakulyanontvittaya, T., Duhl, T., Emmons, L. K., & Wang, X. (2012). The Model of Emissions of Gases and Aerosols from Nature version 2.1 (MEGAN2.1): An extended and updated framework for modeling biogenic emissions. *Geoscientific Model Development*, 5(6), 1471–1492. <https://doi.org/10.5194/gmd-5-1471-2012>

Guo, S., Bluth, G. J. S., Rose, W. I., Watson, I. M., & Prata, A. J. (2004). Re-evaluation of SO<sub>2</sub> release of the 15 June 1991 Pinatubo eruption using ultraviolet and infrared satellite sensors. *Geochemistry, Geophysics, Geosystems*, 5, Q04001. <https://doi.org/10.1029/2003GC000654>

Guo, S., Rose, W. I., Bluth, G. J. S., & Watson, I. M. (2004). Particles in the great Pinatubo volcanic cloud of June 1991: The role of ice. *Geochemistry, Geophysics, Geosystems*, 5, Q05003. <https://doi.org/10.1029/2003GC000655>

Hansen, J., Lacis, A., Ruedy, R., & Sato, M. (1992). Potential climate impact of Mount Pinatubo eruption. *Geophysical Research Letters*, 19(2), 215–218. <https://doi.org/10.1029/91GL02788>

Hansen, J., Ruedy, R., Sato, M., & Lo, K. (2010). Global surface temperature change. *Reviews of Geophysics*, 48, RG4004. <https://doi.org/10.1029/2010RG000345>

Hansen, J., Sato, M., Ruedy, R., Nazarenko, L., Lacis, A., Schmidt, G. A., ... Zhang, S. (2005). Efficacy of climate forcings. *Journal of Geophysical Research*, 110, D18104. <https://doi.org/10.1029/2005JD005776>

Hofmann, D., Barnes, J. E., O'Neill, M., Trudeau, M., & Neely, R. R. III (2009). Increase in background stratospheric aerosol observed with lidar at Mauna Loa Observatory and Boulder, Colorado. *Geophysical Research Letters*, 36, L15808. <https://doi.org/10.1029/2009GL039008>

Holasek, R. E., Self, S., & Woods, A. W. (1996). Satellite observations and interpretation of the 1991 Mount Pinatubo eruption plumes. *Journal of Geophysical Research*, 101(B12), 27,635–27,655. <https://doi.org/10.1029/96JB01179>

Holland, M. M., Bailey, D. A., Briegleb, B. P., Light, B., & Hunke, E. (2012). Improved sea ice shortwave radiation physics in CCSM4: The impact of melt ponds and aerosols on Arctic sea ice. *Journal of Climate*, 25(5), 1413–1430. <https://doi.org/10.1175/JCLI-D-11-00078.1>

Hurrell, J. W., Holland, M. M., Gent, P. R., Ghosh, S., Kay, J. E., Kushner, P. J., ... Marshall, S. (2013). The Community Earth System Model: A framework for collaborative research. *Bulletin of the American Meteorological Society*, 100(4), 1222–1247. <https://doi.org/10.1175/BAMS-D-12-00121>

Ivy, D. J., Solomon, S., Kinnison, D. E., Mills, M. J., Schmidt, A., & Neely, R. R. III (2017). The influence of the Calbuco eruption on the 2015 Antarctic ozone hole in a fully coupled chemistry-climate model. *Geophysical Research Letters*, 23, 2556–2561. <https://doi.org/10.1002/2016GL071925>

Jäger, H., & Deshler, T. (2002). Lidar backscatter to extinction, mass and area conversions for stratospheric aerosols based on midlatitude balloonborne size distribution measurements. *Geophysical Research Letters*, 29(19), 1929. <https://doi.org/10.1029/2002GL015609>

Jäger, H., & Deshler, T. (2003). Correction to "Lidar backscatter to extinction, mass and area conversions for stratospheric aerosols based on midlatitude balloonborne size distribution measurements". *Geophysical Research Letters*, 30(7), 1382. <https://doi.org/10.1029/2003GL017189>

Jones, A. C., Haywood, J. M., Jones, A., & Aquila, V. (2016). Sensitivity of volcanic aerosol dispersion to meteorological conditions: A Pinatubo case study. *Journal of Geophysical Research: Atmospheres*, 121, 6892–6908. <https://doi.org/10.1002/2016JD025001>

Kay, J. E., Deser, C., Phillips, A., Mai, A., Hannay, C., Strand, G., ... Vertenstein, M. (2015). The Community Earth System Model (CESM) large ensemble project: A community resource for studying climate change in the presence of internal climate variability. *Bulletin of the American Meteorological Society*, 96(8), 1333–1349. <https://doi.org/10.1175/BAMS-D-13-00255.1>

Kravitz, B., MacMartin, D. G., Mills, M. J., Richter, J. H., Tilmes, S., Lamarque, J.-F., ... Vitt, F. (2017). First simulations of designing stratospheric sulfate aerosol geoengineering to meet multiple simultaneous climate objectives. *Journal of Geophysical Research: Atmospheres*, 122. <https://doi.org/10.1002/2017JD026874>

Lambert, A., Grainger, R. G., Remedios, J. J., Rodgers, C. D., Corney, M., & Taylor, F. W. (1993). Measurements of the evolution of the Mt. Pinatubo aerosol cloud by ISAMS. *Geophysical Research Letters*, 20(12), 1287–1290. <https://doi.org/10.1029/93GL00827>

Lauritzen, P. H., Bacmeister, J. T., Callaghan, P. F., & Taylor, M. A. (2015). NCAR\_Topo (v1.0): NCAR global model topography generation software for unstructured grids. *Geoscientific Model Development*, 8(12), 3975–3986. <https://doi.org/10.5194/gmd-8-3975-2015>

Lawrence, D. M., Oleson, K. W., Flanner, M. G., Thornton, P. E., Swenson, S. C., Lawrence, P. J., ... Slater, A. G. (2011). Parameterization improvements and functional and structural advances in version 4 of the Community Land Model. *Journal of Advances in Modeling Earth Systems*, 3(3), 45. <https://doi.org/10.1029/2011MS000045>

Lindzen, R. S. (1981). Turbulence and stress owing to gravity wave and tidal breakdown. *Journal of Geophysical Research*, 86(C10), 9707–9714. <https://doi.org/10.1029/JC086iC10p09707>

Liu, C., Allan, R. P., Berrisford, P., Mayer, M., Hyder, P., Loeb, N., ... Edwards, J. M. (2015). Combining satellite observations and reanalysis energy transports to estimate global net surface energy fluxes 1985–2012. *Journal of Geophysical Research: Atmospheres*, 120, 9374–9389. <https://doi.org/10.1002/2015JD023264>

Liu, X., Easter, R. C., Ghan, S. J., Zaveri, R., Rasch, P., Shi, X., ... Mitchell, D. (2012). Toward a minimal representation of aerosols in climate models: Description and evaluation in the Community Atmosphere Model CAM5. *Geoscientific Model Development*, 5(3), 709–739. <https://doi.org/10.5194/gmd-5-709-2012>

Livesey, N. J., Read, W. G., Wagner, P. A., Froidevaux, L., Lambert, A., Manney, G. L., ... Martinez, E. (2016). Aura Microwave Limb Sounder (MLS) version 4.2x level 2 data quality and description document, Tech. Rep. JPL D-33509 Rev. A, Jet Propulsion Laboratory. Retrieved from [https://mls.jpl.nasa.gov/data/v4\\_2\\_data\\_quality\\_document.pdf](https://mls.jpl.nasa.gov/data/v4_2_data_quality_document.pdf), (Accessed 5 January 2016).

MacMartin, D. G., Kravitz, B., Tilmes, S., Richter, J. H., Mills, M. J., Lamarque, J.-F., & Tribbia, J. (2017). The climate response to stratospheric aerosol geoengineering can be tailored using multiple injection locations. *Journal of Geophysical Research: Atmospheres*, 122. <https://doi.org/10.1002/2017JD026868>

Mankin, W. G., Coffey, M. T., & Goldman, A. (1992). Airborne observations of SO<sub>2</sub>, HCl, and O<sub>3</sub> in the stratospheric plume of the Pinatubo Volcano in July 1991. *Geophysical Research Letters*, 19(2), 179–182. <https://doi.org/10.1029/91GL02942>

Marsh, D. R., Mills, M. J., Kinnison, D. E., Lamarque, J.-F., Calvo, N., & Polvani, L. M. (2013). Climate change from 1850 to 2005 simulated in CESM1(WACCM). *Journal of Climate*, 26(19), 7372–7391. <https://doi.org/10.1175/JCLI-D-12-00558.1>

McNutt, M. K., Abdalati, W., Caldeira, K., Doney, S. C., Falkowski, P. G., Fetter, S., ... Wilcox, J. (2015). *Climate intervention: Reflecting sunlight to cool Earth*. Washington, DC: National Academies Press.

McPeters, R. D. (1993). The atmospheric SO<sub>2</sub> budget for Pinatubo derived from NOAA-11 SBUV/2 spectral data. *Geophysical Research Letters*, 20(18), 1971–1974. <https://doi.org/10.1029/93GL02360>

McPeters, R. D., Bhartia, P. K., Haffner, D., Labow, G. J., & Flynn, L. (2013). The version 8.6 SBUV ozone data record: An overview. *Journal of Geophysical Research: Atmospheres*, 118, 8032–8039. <https://doi.org/10.1002/jgrd.50597>

Mills, M. J., Schmidt, A., Easter, R., Solomon, S., Kinnison, D. E., Ghan, S. J., ... Gettelman, A. (2016). Global volcanic aerosol properties derived from emissions, 1990–2014, using CESM1(WACCM). *Journal of Geophysical Research: Atmospheres*, 121, 2332–2348. <https://doi.org/10.1002/2015JD024290>

Minnis, P., Harrison, E. F., Stowe, L. L., Gibson, G. G., Denn, F. M., Doelling, D. R., & Smith, W. L. (1993). Radiative climate forcing by the Mount Pinatubo eruption. *Science*, 259(5100), 1411–1415. <https://doi.org/10.1126/science.259.5100.1411>

Mote, P. W., Rosenlof, K. H., McIntyre, M. E., Carr, E. S., Gille, J. C., Holton, J. R., ... Waters, J. W. (1996). An atmospheric tape recorder: The imprint of tropical tropopause temperatures on stratospheric water vapor. *Journal of Geophysical Research*, 101(D2), 3989–4006. <https://doi.org/10.1029/95JD03422>

Myhre, G., Shindell, D., Bréon, F. M., Collins, W., Fuglestvedt, J., Huang, J., ... Zhang, H. (2013). Anthropogenic and natural radiative forcing. In T. F. Stocker et al. (Eds.), *Climate change 2013: The physical science basis. Contribution of Working Group I to the Fifth Assessment Report of the Intergovernmental Panel on Climate Change* (Chap. 8, pp. 659–740). Cambridge, United Kingdom and New York: Cambridge University Press.

Neale, R. B., Gettelman, A., Park, S., Conley, A. J., Kinnison, D., Marsh, D., ... Rasch, P. J. (2010). Description of the NCAR Community Atmosphere Model (CAM 5.0). NCAR Tech. Rep. NCAR/TN-4861STR.

Neely, R. R. III, Conley, A. J., Vitt, F., & Lamarque, J.-F. (2016). A consistent prescription of stratospheric aerosol for both radiation and chemistry in the Community Earth System Model (CESM1). *Geoscientific Model Development*, 9(7), 2459–2470. <https://doi.org/10.5194/gmd-9-2459-2016>

Neely, R. R. III, & Schmidt, A. (2016). VolcanEESM: Global volcanic sulphur dioxide (SO<sub>2</sub>) emissions database from 1850 to present—Version 1.0. <https://doi.org/10.5285/76ebdc0b-0eed-4f70-b89e-55e606bcd568>

Niemeier, U., Timmreck, C., Graf, H. F., Kinne, S., Rast, S., & Self, S. (2009). Initial fate of fine ash and sulfur from large volcanic eruptions. *Atmospheric Chemistry and Physics*, 9(22), 9043–9057. <https://doi.org/10.5194/acp-9-9043-2009>

Pinto, J. P., Toon, O. B., & Turco, R. P. (1989). Self-limiting physical and chemical effects in volcanic eruption clouds. *Journal of Geophysical Research*, 94(D8), 11165. <https://doi.org/10.1029/JD094iD08p11165>

Pitari, G., Aquila, V., Kravitz, B., Robock, A., Watanabe, S., Cionni, I., ... Tilmes, S. (2014). Stratospheric ozone response to sulfate geoengineering: Results from the Geoengineering Model Intercomparison Project (GeoMIP). *Journal of Geophysical Research: Atmospheres*, 119, 2629–2653. <https://doi.org/10.1002/2013JD020566>

Pitari, G., Cionni, I., Di Genova, G., Visioni, D., Gandolfi, I., & Mancini, E. (2016). Impact of stratospheric volcanic aerosols on age-of-air and transport of long-lived species. *Atmosphere*, 7(11), 149. <https://doi.org/10.3390/atmos7110149>

Pitari, G., Di Genova, G., Mancini, E., Visioni, D., Gandolfi, I., & Cionni, I. (2016). Stratospheric aerosols from major volcanic eruptions: A composition–climate model study of the aerosol cloud dispersal and e-folding time. *Atmosphere*, 7(6), 75–21. <https://doi.org/10.3390/atmos7060075>

Portmann, R. W., Solomon, S., Garcia, R. R., Thomason, L. W., Poole, L. R., & McCormick, M. P. (1996). Role of aerosol variations in anthropogenic ozone depletion in the polar regions. *Journal of Geophysical Research*, 101(D17), 22,991–23,006. <https://doi.org/10.1029/96JD02608>

Raible, C. C., Brönnimann, S., Auchmann, R., Brohan, P., Frölicher, T. L., Graf, H.-F., ... Wegmann, M. (2016). Tambora 1815 as a test case for high impact volcanic eruptions: Earth system effects. *WIREs Climate Change*, 7(4), 569–589. <https://doi.org/10.1002/wcc.407>

Read, W. G., Froidevaux, L., & Waters, J. W. (1993). Microwave limb sounder measurement of stratospheric SO<sub>2</sub> from the Mt. Pinatubo Volcano. *Geophysical Research Letters*, 20(12), 1299–1302. <https://doi.org/10.1029/93GL00831>

Richter, J. H., Sassi, F., & Garcia, R. R. (2010). Toward a physically based gravity wave source parameterization in a general circulation model, 67(1), 136–156. <https://doi.org/10.1175/2009JAS3112.1>

Richter, J. H., Solomon, A., & Bacmeister, J. T. (2014). On the simulation of the quasi-biennial oscillation in the community atmosphere model, version 5. *Journal of Geophysical Research: Atmospheres*, 119, 3045–3062. <https://doi.org/10.1002/2013JD021122>

Richter, J. H., Tilmes, S., Mills, M. J., Tribbia, J., Kravitz, B., MacMartin, D. G., ... Lamarque, J.-F. (2017). Stratospheric dynamical response to SO<sub>2</sub> injections. *Journal of Geophysical Research: Atmospheres*, 122. <https://doi.org/10.1002/2017JD026912>

Ridley, D. A., Solomon, S., Barnes, J. E., Burlakov, V. D., Deshler, T., Dolgii, S. I., ... Vernier, J. P. (2014). Total volcanic stratospheric aerosol optical depths and implications for global climate change. *Geophysical Research Letters*, 41, 7763–7769. <https://doi.org/10.1002/2014GL061541>

Rienecker, M. M., Suarez, M. J., Gelaro, R., Todling, R., Bacmeister, J., Liu, E., ... Woollen, J. (2011). MERRA: NASA's Modern-Era Retrospective Analysis for Research and Applications. *Journal of Climate*, 24(14), 3624–3648. <https://doi.org/10.1175/JCLI-D-11-00015.1>

Robock, A. (2000). Volcanic eruptions and climate. *Reviews of Geophysics*, 38(2), 191–219. <https://doi.org/10.1029/1998RG000054>

Sekiya, T., Sudo, K., & Nagai, T. (2016). Evolution of stratospheric sulfate aerosols from the 1991 Pinatubo eruption: Roles of aerosol microphysical processes. *Journal of Geophysical Research: Atmospheres*, 121, 2911–2938. <https://doi.org/10.1002/2015JD024313>

Sheng, J. X., Weisenstein, D. K., Luo, B. P., Rozanov, E., Arfeuille, F., & Peter, T. (2015). A perturbed parameter model ensemble to investigate Mt. Pinatubo's 1991 initial sulfur mass emission. *Atmospheric Chemistry and Physics*, 15(20), 11,501–11,512. <https://doi.org/10.5194/acp-15-11501-2015>

Shi, X., Liu, X., & Zhang, K. (2015). Effects of pre-existing ice crystals on cirrus clouds and comparison between different ice nucleation parameterizations with the Community Atmosphere Model (CAM5). *Atmospheric Chemistry and Physics*, 15(3), 1503–1520. <https://doi.org/10.5194/acp-15-1503-2015>

Smith, K. L., Neely, R. R. III, Marsh, D. R., & Polvani, L. M. (2014). The Specified Chemistry Whole Atmosphere Community Climate Model (SC-WACCM). *Journal of Advances in Modeling Earth Systems*, 6(3), 883–901. <https://doi.org/10.1002/2014MS000346>

Soden, B. J., Wetherald, R. T., Stenchikov, G. L., & Robock, A. (2002). Global cooling after the eruption of Mount Pinatubo: A test of climate feedback by water vapor. *Science*, 296(5658), 727–730. <https://doi.org/10.1126/science.296.5658.727>

Solomon, S., Hy, D. J., Kinnison, D. E., Mills, M. J., Neely, R. R. III, & Schmidt, A. (2016). Emergence of healing in the Antarctic ozone layer. *Science*, 353(6296), 269–274, aae0061–274. <https://doi.org/10.1126/science.aae0061>

Solomon, S., Kinnison, D. E., Bandoro, J., & Garcia, R. R. (2015). Simulation of polar ozone depletion: An update. *Journal of Geophysical Research: Atmospheres*, 120, 7958–7974. <https://doi.org/10.1002/2015JD023365>

Swinbank, R., & Ortland, D. A. (2003). Compilation of wind data for the Upper Atmosphere Research Satellite (UARS) reference atmosphere project. *Journal of Geophysical Research*, 108, 4615. <https://doi.org/10.1029/2002JD003135>

Tilmes, S., Richter, J. H., Mills, M. J., Kravitz, B., Vitt, F., Tribbia, J., & Lamarque, J.-F. (2017). Sensitivity of aerosol distribution and climate response to stratospheric SO<sub>2</sub> injection locations. *Journal of Geophysical Research: Atmospheres*, 122. <https://doi.org/10.1002/2017JD026888>

Timmreck, C., Graf, H. F., & Feichter, J. (1999). Simulation of Mt. Pinatubo volcanic aerosol with the Hamburg climate model ECHAM4. *Theoretical and Applied Climatology*, 62(3-4), 85–108. <https://doi.org/10.1007/s007040050076>

Timmreck, C., Graf, H.-F., & Kirchner, I. (1999). A one and half year interactive MA/ECHAM4 simulation of Mount Pinatubo aerosol. *Journal of Geophysical Research*, 104(D8), 9337–9359. <https://doi.org/10.1029/1999JD900088>

Trepte, C. R., & Hitchman, M. H. (1992). Tropical stratospheric circulation deduced from satellite aerosol data. *Nature*, 355(6361), 626–628. <https://doi.org/10.1038/355626a0>

Visioni, D., Pitari, G., & Aquila, V. (2017). Sulfate geoengineering: A review of the factors controlling the needed injection of sulfur dioxide. *Atmospheric Chemistry and Physics*, 17(6), 3879–3889. <https://doi.org/10.5194/acp-17-3879-2017>

Williamson, D. L., Olson, J. G., Hannay, C., Toniazzo, T., Taylor, M., & Yudin, V. (2015). Energy considerations in the Community Atmosphere Model (CAM). *Journal of Advances in Modeling Earth Systems*, 7(3), 1178–1188. <https://doi.org/10.1002/2015MS000448>

Wood, G. D. (2014). *Tambora* (312 pp.). Princeton and Oxford: Princeton University Press.

Xu, J., Smith, A. K., Yuan, W., Liu, H. L., Wu, Q., Mlynczak, M. G., & Russell, J. M. (2007). Global structure and long-term variations of zonal mean temperature observed by TIMED/SABER. *Journal of Geophysical Research*, 112, D24106. <https://doi.org/10.1029/2007JD008546>

Ziemke, J. R., Chandra, S., Labow, G. J., Bhartia, P. K., Froidevaux, L., & Witte, J. C. (2011). A global climatology of tropospheric and stratospheric ozone derived from Aura OMI and MLS measurements. *Atmospheric Chemistry and Physics*, 11(17), 9237–9251. <https://doi.org/10.5194/acp-11-9237-2011>

Zuev, V. V., Burlakov, V. D., Nevezorov, A. V., Pravdin, V. L., Savelieva, E. S., & Gerasimov, V. V. (2016). 30-year lidar observations of the stratospheric aerosol layer state over Tomsk (Western Siberia, Russia). *Atmospheric Chemistry and Physics Discussions*, 1–25, 1–25. <https://doi.org/10.5194/acp-2016-792>